Journal of Ocean Engineering and Marine Energy (2026) 12:837–866
https://doi.org/10.1007/s40722-025-00464-z

RESEARCH

Performance of a floating wind turbine with a centreboard and heave plate at two North Sea sites: a numerical evaluation informed by experimental findings

Diego F. Bernal-Camacho[1,3] · Edgar Mendoza[1] · Jassiel V. H. Fontes[2] · Antonis I. Vakis[3]

Received: 25 June 2025 / Accepted: 27 December 2025 / Published online: 31 January 2026

Abstract
A floating offshore wind turbine (FOWT) offers a solution for harnessing wind energy in extensive offshore areas far from the coast; however, evaluating its motions under combined wave and wind conditions presents challenges. The present study numerically assesses the effectiveness of a passive motion reduction system, previously tested experimentally, consisting of a centreboard and a heave plate, in sea conditions at two sites in the North Sea that differ in energy. The performance of the OC4 DeepCwind semi-submersible platform is investigated using WEC-Sim and MOST, both with and without the motion reduction system. The results indicate reduced surge, heave, and pitch motions, along with decreased tower base and blade root loads, resulting in increased power output. These findings demonstrate the system's capacity to enhance platform performance in offshore environments, thereby advancing floating wind technology.

Keywords FOWT · Wind energy · North Sea · Motion reduction system · WEC-Sim

1 Introduction

The deployment of floating offshore wind turbines (FOWT) enables harnessing significant wind energy resources in ocean regions where fixed-bottom structures would be impractical (Keivanpour et al. 2017). Wind energy is a key component of international climate goals, set out in the Paris Agreement and the Glasgow Climate Pact. Global offshore wind capacity is expected to grow from 500 GW in 2030 to about 2465 GW by 2050. Although offshore wind installations remain more expensive than onshore alternatives, the declining levelized cost of energy in recent years has increased their appeal to investors. Global offshore capacity reached 64.3 GW in 2022, with 8.8 GW added that year, primarily driven by China, the United Kingdom, Germany, The Netherlands, and Denmark (IRENA and GWEC 2023; Martinez and Iglesias 2024). In Europe, onshore wind generation still exceeds offshore production; however, marine installations offer distinct advantages. Onshore projects often encounter social opposition due to environmental, economic, and visual impacts. In contrast, offshore turbines, located far from coastal areas, face fewer constraints and benefit from stronger and more consistent wind resources (Enevoldsen et al. 2019). For that reason, advances in technology and the growing interest in deeper water sites have expanded offshore wind potential (Hong et al. 2024). Approximately a decade ago, wind turbines were installed around 5 km from the coastline; by 2010, this distance had increased to 30 km. Current plans involve installing them at locations up to 200 km from the coast and at depths of up to 175 m. In such conditions, FOWTs present a compelling alternative (Sovacool and Enevoldsen 2015). However, their operation in marine environments introduces significant challenges. For example, motions induced by waves and wind can compromise stability, leading to excessive translational and angular motions that may affect operational activities and threaten structural integrity. This is because the hydrodynamic and aerodynamic

✉ Antonis I. Vakis
a.vakis@rug.nl

1 Instituto de Ingeniería, Universidad Nacional Autónoma de México, Mexico City, Mexico

2 Departamento de Engenharia Naval, Escola Superior de Tecnologia, Universidade do Estado do Amazonas, Manaus, Brazil

3 Computational Mechanical and Materials Engineering, Engineering and Technology Institute Groningen, Faculty of Science and Engineering, University of Groningen, Groningen, The Netherlands

loads could increase fatigue stresses on the tower, blades, and mooring lines, thereby reducing the platform's lifetime. Furthermore, the resulting motion oscillations may impact the efficiency of energy conversion, as variations in rotor inclination and relative wind velocity can affect control system strategies and power output (Collu et al. 2014; Chitteth Ramachandran 2022, Hong et al. 2024).

Despite the benefits of installing FOWTs in areas with wind potential, the challenges previously discussed need to be addressed; hence, a range of motion reduction strategies for FOWTs have been analysed. For example, Passive Damping Systems (PDS), as examined by Borg et al. (2013), include bottom plates, passive anti-roll tanks, and open-bottom tanks, which enhance hydrodynamic platform performance. Different mooring line configurations, such as catenary, semi-taut, and taut systems, also function as PDS by maintaining the platform within a specific range, stabilising and mitigating platform motions (Timmington and Efthimiou 2022). Zhao et al. (2012) analysed the effect of varying catenary mooring line tension on the response of a FOWT under various sea conditions. They found that the aerodynamic loads on the rotor significantly influence the platform's motion and that a properly designed mooring line can support dynamic stability and reduce motions. On the other hand, Active Control Systems (ACS) focus on real-time adjustments to platform motions. For instance, Capaldo and Mella (2022) proposed a control strategy that adjusts the blade pitch according to the platform's pitch inclination. Meanwhile, Stockhouse et al. (2022) explored a different approach to ACS by integrating blade pitch and torque control to reduce platform tilting and enhance power generation. Another alternative is hybrid systems; Zhu et al. (2020) studied the integration of wave energy converters in an FOWT, which offers the dual benefits of motion reduction and supplementary energy generation. A different hybrid approach, analysed by Aboutalebi et al. (2023), involved strategically placing oscillating water column systems to enhance platform motions. Although several studies have provided valuable insights into motion reduction strategies for FOWT, certain limitations remain. Many analyses have been conducted under simplified or generic sea states, without accounting for site-specific environmental variability. Furthermore, a few studies have conducted parametric sensitivity analyses to assess the impact of variations in underwater geometry on platform stability. Closing these gaps is essential to better understanding PDS performance under specific offshore conditions.

The above-mentioned motion reduction systems present distinct advantages and limitations. It is evident that ACSs provide effective motion mitigation for floating platforms. Nevertheless, it should be noted that their implementation necessitates a considerable financial investment, and their components require regular maintenance. Hybrid systems, such as wave energy converters, have been shown to incur greater expense (Guo et al. 2023) due to their integration of different technologies for motion reduction and power generation. Additionally, their operation demands complex control mechanisms to ensure optimal efficiency and reliability. On the other hand, PDS, despite its lack of real-time adjustability, offer a straightforward and cost-effective option with minimal maintenance demands. These systems demonstrate notable efficacy across a broad spectrum of sea conditions. Nonetheless, their implementation must be subjected to rigorous evaluation under various environmental conditions to ensure its suitability before deployment. For example, Bernal-Camacho et al. (2024) conducted experimental research on the motion of an FOWT with a PDS composed of a centreboard and heave plate, in an enclosed wind-wave environment. This demonstrated the system's effectiveness in reducing translational and rotational motion. However, the previous study was limited to analysing platform motion using a single PDS configuration and sea conditions representative of a single location in the Gulf of Tehuantepec. Therefore, the present investigation builds upon the former work by extending the study to include a numerical analysis of different PDS configurations under environmental conditions from two North Sea sites. The first configuration replicates the previously tested design, featuring a rectangular centreboard with a circular heave plate attached to its base and mounted on the platform's central column. Two additional configurations introduce variations in the heave plate diameter and centreboard length to modify the platform stability. The objective is to evaluate the platform's surge, heave, and pitch motions, along with the corresponding mooring line forces, tower base and blade root loads, and power output of a semi-submersible platform supporting a 5 MW wind turbine. It is hypothesised that minimising platform motions could enhance structural reliability and power output, which is critical for the platform's economic viability (Dagher et al. 2024; Yang et al. 2023). In addition, unlike previous studies that modified the column (Zhao et al. 2024) or heave plate shapes (Li et al. 2024; Gonçalves et al. 2023) and test it under generic sea conditions, our study assessed the centreboard and heave plate using site-specific wave and wind ERA5 data from two locations with offshore wind potential in the Dutch and United Kingdom Exclusive Economic Zones (EEZ) in the North Sea. The platform's motions are evaluated numerically using the Wave Energy Converter Simulator (WEC-Sim) (Kelley Ruehl et al. 2024) and the Matlab for Offshore Simulation Tool (MOST) for the wind turbine (Sirigu et al. 2022) to simulate the combined effects of hydrodynamic and aerodynamic loads.

The structure of the paper is as follows: First, we analysed the sea conditions at two sites in the North Sea. Next, we designed the FOWT, including the centreboard and heave plate configurations. The hydrodynamic coefficients for the

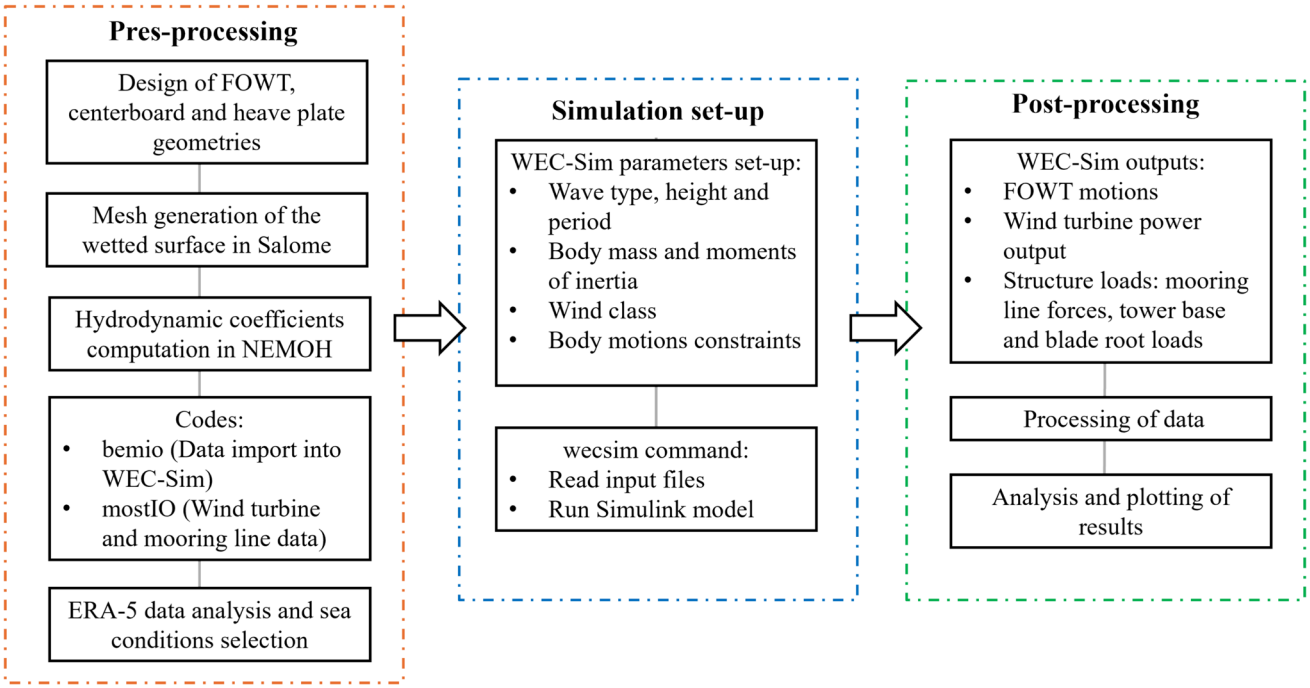

Fig. 1 Methodology flowchart for the FOWT numerical model simulations

platform were obtained using NEMOH and utilised in WEC-Sim. The characteristics of the 5 MW wind turbine were defined in MOST for the platform's time-domain simulations. The results of the platform, both with and without the PDS are presented and discussed in various sea conditions. The key findings of the study are highlighted in relation to how the centreboard and heave plate enhance platform performance.

2 Methodology

The methodology flowchart of this study is illustrated in Fig. 1. It is divided into three stages: pre-processing, simulation set-up, and post-processing. In the pre-processing stage, the FOWT, centreboard, and heave plate geometries were designed in CAD software. The wetted surface of each configuration was then exported as an STEP file and meshed in Salome (EDF and CEA 2022) to generate an STL file employed to compute the hydrodynamic coefficients in NEMOH (Kurnia and Ducrozet 2022) and subsequently imported into WEC-Sim using the boundary element method input/output code (bemio) for time-domain simulations. The mostIO module was used to generate look-up tables for the wind turbine and mooring system, which are retrieved during simulations based on the defined incoming wave and wind specifications. Additionally, representative sea conditions from two North Sea sites were identified through the analysis of ERA5 data. In the simulation set-up, WEC-Sim parameters were defined, such as regular waves along with their height and period, body mass, and moments of inertia. A constant wind flow was applied, and the platform motion was constrained to surge, heave, and pitch motions. The simulation was run with the wecsim command to process the input files and the Simulink model. In the post-processing stage, the results of the platform motions, power output, and structural loads on the mooring system, tower base, and blade root were processed, analysed, and plotted. Further details on each step are provided in this section.

2.1 Sea conditions analysis at two North Sea sites

The North Sea region has been identified as having sufficient wind energy potential to facilitate the transition towards a renewable future. The Netherlands and the United Kingdom will need to expand their offshore wind energy installations to meet their national energy targets. Both countries have EEZs with considerable wind energy potential, suitable for deploying either fixed or floating wind turbines, depending on water depth. The relatively short distances from the coast to cities, combined with declining offshore wind energy costs, may enhance the harnessing of wind power in these areas. Two sites within the EEZ of the Netherlands and the United Kingdom were selected for analysis of their sea conditions. The analysis utilises ERA (Hersbach et al. 2020) data spanning 44 years, from 1980 to 2023. The map in Fig. 2, elaborated in QGIS 3.28 using layers from Porto Tapiquen (2017), the Netherlands Ministry of Defence (2025), and the Flanders

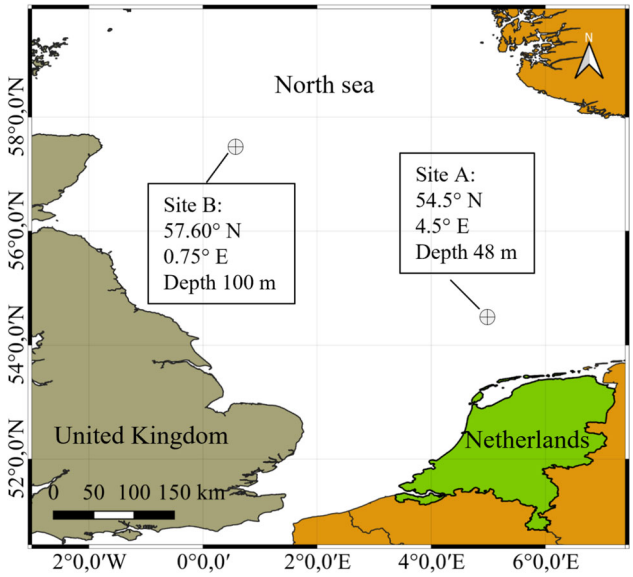

Fig. 2 Offshore location map of the sea conditions at two sites in the North Sea

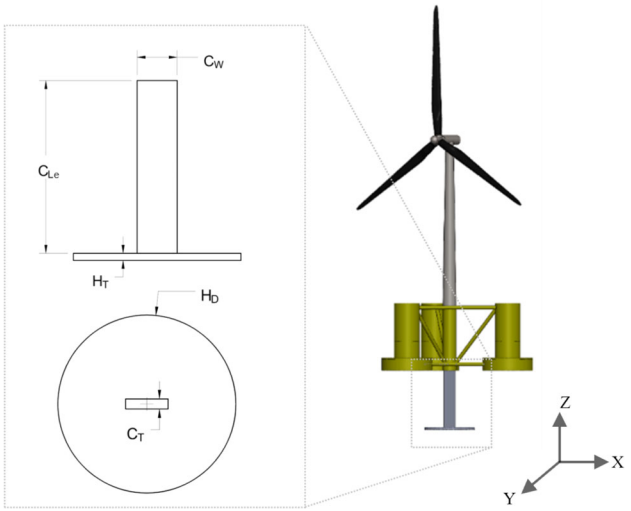

Fig. 3 Scheme of the motion reduction system, showing the centreboard and heave plate details and their location in the FOWT

Marine Institute (2025), illustrates the locations of interest. Site A is approximately 142 km northwest of Ameland, located near the German EEZ border. This area is projected to produce around 4000 MW of wind energy (Government.nl 2024). Site B is located approximately 176 km east-northeast of Aberdeen, United Kingdom, and has been identified for wind farm development (WSP UK Limited 2025).

The ERA5 data include wave direction, significant wave height (Hs), peak wave period (Tp), wind velocity (WV), and wind direction. To statistically analyse this information, an annual joint probability plot of Tp and Hs, along with WV, was generated and is presented in the Results and discussion section. This information highlights the relationship between these variables and facilitates the selection of representative sea conditions for testing the FOWT's performance.

2.2 Platform with centreboard and heave plate motion reduction system

The semi-submersible OC4 DeepCwind platform, designed for offshore wind turbines, was used in this work to numerically test a PDS. This platform features a central column that supports the wind turbine tower. This column is connected to three outer columns by pontoons, forming a symmetric structure (Robertson et al. 2014). To evaluate its performance, a motion reduction system was integrated into the platform. This system consisted of two components designed to mitigate platform motions. A vertical rectangular centreboard attached to the platform's central column to reduce surge displacements and a circular heave plate affixed to the centreboard base to reduce heave displacements, both aiming to increase wetted surface area and contributing additional damping. These two components could diminish the pitch motion (Bernal-Camacho et al. 2024; Yang et al. 2024; Subbulakshmi and Sundaravadivelu 2021). Moreover, the PDS system's location and geometry modify stability by lowering the centre of gravity, thereby increasing the metacentric height, which could help reduce pitch motion and influence wind turbine operability across distinct marine environments.

This study examines three system configurations: the centreboard and heave plate (CH) configuration and two modified versions of this: one with a larger diameter heave plate (CHL) and one with a shorter centreboard (CHS). The thickness of the heave plate (H_T), the width of the centreboard (C_W), and its thickness (C_T) are consistently 1.02 m, 6.4 m, and 0.68 m across the three configurations, respectively. The C_W corresponds to the diameter of the platform's central column, which has a rectangular downward extension designed to increase its underwater surface area. The H_T and C_T thicknesses were chosen to increase the platform's mass and draft, thereby lowering its centre of gravity and altering its stability properties. These geometric parameters, treated at full scale in this study, are the same as those used in Bernal-Camacho et al. (2024), which demonstrated favourable motion reduction performance with the CH configuration. However, the centreboard length (C_{Le}) and the heave plate diameter (HD) were varied. The CHS features a C_{Le} that is half the size, whilst the H_D of the CHL was increased by around 8%. These modifications were implemented to assess their influence on platform motions and to gain further insight into the effects of different centreboard and heave plate dimensions. Figure 3 illustrates the motion reduction system components and location in the FOWT; the dimensions are detailed in Table 1.

Table 1 Dimensions of the three motion reduction system configurations installed on the platform

Configuration	C_{Le} (m)	H_D (m)
CH	27.2	23.8
CHL	27.2	25.8
CHS	13.6	23.8

Table 2 displays the properties of the four platform configurations used in the numerical simulations (obtained in SolidWorks), including the centre of gravity (CG), the centre of buoyancy (CB), mass, draft, and moments of Inertia about the *X*-, *Y*-, and *Z*-axes labelled as *Ixx*, *Iyy*, and *Izz*, respectively. It is important to note that at site A, the depth is 48 m; thus, only the FOWT designs without CH and with CHS were simulated due to depth restrictions for the other configurations. At site B, the 100 m water depth allows for simulating the FOWT without CH and with CH, CHS, and CHL.

2.3 Offshore wind turbine specifications

This study utilises the standardised 5 MW wind turbine design by the National Renewable Energy Laboratory; its main specifications are presented in Table 3**,** developed for offshore wind energy (Jonkman et al. 2009). The turbines' blade and rotor properties were employed without modification and used in MOST to analyse its performance on a floating platform. The three-bladed rotor operates with torque and blade pitch control. In this study, the ROSCO control (Abbas et al. 2022) is used in MOST.

The blade cross-section comprises eight aerofoils distributed along the blade span. The first two aerofoil configurations near the root are cylindrical and generate no lift. Thus, the information of the remaining six aerofoils was used to assess the wind turbine's performance. These include aerofoils from Delft University of Technology and the National Advisory Committee for Aeronautics, labelled as DU and NACA, respectively. In the DU aerofoils, the first two numbers indicate relative thickness as a percentage of chord length. For NACA aerofoils, the "6" refers to the series, and the "4" indicates the location of the minimum pressure along the chord, in this case, at 40% of the leading edge (Anderson 2011). The suffix "A17" denotes the aspect ratio of the aerofoil shape. The aerofoil number, type, chord (C), twist angle, section length (S), lift coefficient (C_L), drag coefficient (C_D), and radial distance (R_d) from the rotor centre are listed in Table 4.

Table 3 Prototype scale specifications of the 5 MW wind turbine

Description	Value
Rated power	5 MW
Rotor diameter without blade precone	126 m
Hub height	90 m
Cut-in-WV	3 m/s
Rated WV	11.4 m/s
Rated generator torque	43.093 kN m
Cut-out-WV	25 m/s
Blade length	61.5 m
Rotor speed	6.9 to 12.1 RPM
Swept area	12,469 m^2
Maximum power coefficient (Cp)	0.482
Optimal tip–speed ratio (TSR)	7.55

2.3.1 Rotor blade theory

The aerodynamic performance and influence on the platform motions of the 5 MW rotor were analysed with MOST within WEC-Sim, which uses rotor blade theory, also known as blade element momentum theory, which assumes a steady wind flow. This approach divides the turbine blade into two-dimensional aerofoil annulus sections, which generate lift forces that spin the rotor and produce mechanical energy in the generator. Each aerofoil section contributes to the lift, drag, thrust, torque, and power output of the wind turbine. In this way, the rotor's rotational speed (W_R) in revolutions per

Table 2 Platform properties without CH, with CH, CHL, and CHS

Properties	Units	Without CH	With CH	With CHL	With CHS
CG	m	9.96	12.94	13.39	12.25
CB	m	13.43	15.49	15.83	14.87
Mass	kg	14.27E + 06	14.85E + 06	14.93E + 06	14.79E + 06
Draft	m	20	21.65	21.9	21.5
Ixx	kg m^2	1.12E + 10	1.18E + 10	1.19E + 10	1.15E + 10
Iyy	kg m^2	1.12E + 10	1.19E + 10	1.20E + 10	1.15E + 10
Izz	kg m^2	1.19E + 10	1.21E + 10	1.21E + 10	1.20E + 10

Table 4 Specifications of the blade aerofoil sections

Number	Aerofoil type	C (m)	Twist angle	S (m)	C_L	C_D	R_d (m)
1	DU40_A17	4.557	13.308	4.1	1.538	0.1288	11.75
2	DU35_A17	4.652	11.480	4.1	1.609	0.0227	15.85
3	DU35_A17	4.458	10.162	4.1	1.475	0.0156	19.95
4	DU30_A17	4.249	9.011	4.1	1.39	0.0155	24.05
5	DU25_A17	4.007	7.795	4.1	1.336	0.0153	28.15
6	DU25_A17	3.748	6.544	4.1	1.208	0.0117	32.25
7	DU21_A17	3.502	5.361	4.1	1.145	0.0103	36.35
8	DU21_A17	3.256	4.188	4.1	0.996	0.0053	40.45
9	NACA64_A17	3.010	3.125	4.1	0.784	0.0053	44.55
10	NACA64_A17	2.764	2.319	4.1	0.72	0.0053	48.65
11	NACA64_A17	2.518	1.526	4.1	0.6	0.0054	52.7
12	NACA64_A17	2.313	0.863	2.7333	0.556	0.0052	56.16
13	NACA64_A17	2.086	0.370	2.7333	0.442	0.0052	58.9
14	NACA64_A17	1.419	0.106	2.7333	0.442	0.0052	61.63

minute is converted to angular velocity (ω) as follows:

$$\omega = \frac{2\pi W_R}{60}. \tag{1}$$

The tangential velocity v_t of the aerofoil blade is calculated as

$$v_t = \omega R_d. \tag{2}$$

Subsequently, the resultant relative velocity (v_r) felt by the blade is obtained by

$$v_r = \sqrt{{v_u}^2 + {v_t}^2}. \tag{3}$$

Here, v_u is the wind velocity upstream.

The lift (L_F) and drag (D_F) forces are calculated by the following equations:

$$L_F = \frac{1}{2}\rho_a {v_r}^2 c C_L S, \tag{4}$$

$$D_F = \frac{1}{2}\rho_a {v_r}^2 c C_D S, \tag{5}$$

where ρ_a is the air density.

The thrust force (T_r), torque (Q), and power output (P) of the blade are computed as

$$T_r = \frac{1}{2}\rho_a {v_r}^2 B c (C_L \mathrm{Cos(Twist)} + C_D \mathrm{Sin(Twist)}) S, \tag{6}$$

$$Q = \frac{1}{2}\rho_a {v_r}^2 B c R_d (C_L \mathrm{Sin(Twist)} - C_D \mathrm{Cos(Twist)}) S, \text{ and} \tag{7}$$

$$P = Q\omega, \tag{8}$$

where B is the number of blades on the rotor. Further details about the rotor blade theory, briefly described from Eqs. (1) to (8), can be found in Burton et al. (2001).

The pitch-bending moment at the tower base is included in the results section. It is determined by multiplying the aerodynamic thrust force exerted on the rotor by the distance from the hub to the point where the tower connects to the platform. Additionally, the blade root pitch moment, which comprises the sectional moments generated by the aerofoil along the blade's span, is included. The locations of the tower base, blade root, and aerofoil sections in the FOWT are illustrated in Fig. 4.

2.3.2 Platform catenary mooring line system forces

The mooring line system forces influencing the FOWT are calculated using catenary equations within a multisegmented quasi-static model in MOST, which internally utilises the mooring analysis programme library to generate look-up tables. In this model, a single catenary mooring line is defined and angularly equally spaced, connected by anchor and fairlead nodes, as illustrated in Fig. 4. This enables the modelling of different mooring geometries, line seabed contact, and three-dimensional force components, assuming that the mooring lines are in static equilibrium, meaning that the lines' dynamic effects, such as inertia, internal damping, and hydrodynamic drag, are neglected (Masciola et al. 2013). The tables are retrieved according to the platform motion at each time step. The catenary mooring line properties defined in Robertson et al. (2014) were implemented in MOST. They are shown in Table 5 for sites A and B, whilst the mooring

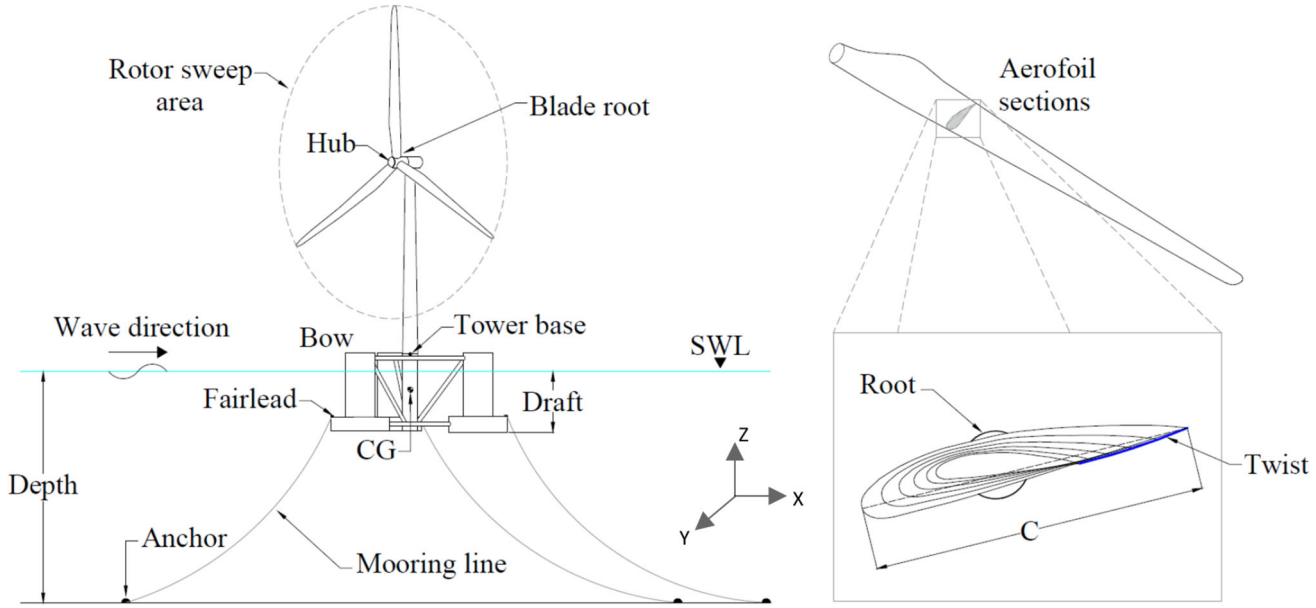

Fig. 4 FOWT, blade, and mooring line system details, along with the tower base and blade root load location points

Table 5 Properties of the catenary mooring line system

Properties	Value
Number of mooring lines	3
Angular separation	120°
Mooring line diameter	0.076 m
Mooring line stiffness	753.6 MN
Line mass density	113.5 kg/m
Unstretched length—Site A	115.2 m
Horizontal fairlead–anchor distance-Site A	109.3 m
Unstretched length-Site B	835.5 m
Horizontal fairlead–anchor distance-Site B	796.7 m

restoring forces in surge, heave, and pitch directions for both mooring systems are provided in Appendix 4.

In this study, the resultant force (F_R) in the surge (F_x) and heave (F_z) directions, as well as its angle (θ) to the mooring line system's origin frame of reference (CG), are computed using Eqs. (9) and (10), respectively. Angle θ is measured from the front of the platform (Bow), starting at the sea water line (SWL) in an anticlockwise direction

$$F_R = \sqrt{F_X{}^2 + F_Z{}^2}. \tag{9}$$

$$\theta = \tan^{-1}\left(\frac{F_Z}{F_X}\right). \tag{10}$$

Figure 4 illustrates the FOWT specifications from Table 2, including the CG and draft, as well as the wind turbine components, such as the hub, blade, and rotor swept area, described in Table 3. The figure also presents a cross-sectional view of the blade showing the aerofoil, including the root, twist, and chord, as detailed in Table 4. Additionally, the mooring line system and locations where tower base and blade root loads are measured are illustrated for clarity.

2.4 Hydrodynamic coefficients calculation in NEMOH

The full-scale design of the platform was developed in SolidWorks 2023 SP02.1 (version 31.2.11) following the specifications outlined by Robertson et al. (2014)**.** The preliminary stage involved creating a detailed STL file of the platform geometry for subsequent meshing processes. The meshing was performed in Salome v.9.9.0 2022 with the aim of capturing surface details of the structure. Then, the STL file was processed through BemRosetta version beta 2024041023 to convert it into a DAT file format. The interaction between waves and the platform was analysed using the boundary element method, employing NEMOH v3.0.0 2022, which applies linear potential flow theory. This analysis aimed to assess the platform's performance across various wave frequencies and to determine hydrodynamic coefficients, including added mass, radiation damping, and response amplitude operators (RAOs). Linear potential flow theory assumes the characteristics of an ideal fluid: irrotational ($\nabla \times v = 0$), inviscid, and incompressible, with constant gravity. In this model, fluid flow is represented by a scalar potential function, Φ. Consequently, the fluid velocity (v) within the flow can be computed as the gradient of

this potential, expressed as $v = \nabla\Phi$. The primary governing equation in linear potential flow is Laplace's equation, $\nabla^2\Phi = 0$, which indicates that the scalar potential is uniformly distributed throughout the fluid domain. For further details on this subject, please refer to Newman (2018).

A mesh dependency study was conducted using three distinct mesh configurations for the FOWT, without CH, with CH, CHL, and CHS, to determine the optimal mesh. The simulations were carried out for wave frequencies ranging from 0.05 to 12 rad/s, with waves approaching the platforms' bow unidirectionally from 0° in a water depth of 100 m. The water density used is 1025 kg/m^3, and the gravitational constant is 9.81 m/s^2. The results from NEMOH obtained in this study were compared with those published by Robertson et al. (2014) using the WAMIT software. First, the cross-correlation (R) was computed for the surge, heave, and pitch-added mass signals to assess their shape and pattern similarities, which is given by Eq. (11), where k is the lag, n is the signal number, N is the total number of samples, and N_e and W are the corresponding values from NEMOH and WAMIT, respectively. Additionally, the root-mean-square error (RMSE) was calculated using Eq. (12) to assess the similarity in magnitude

$$R(k) = \sum_{n=1}^{N-1} (N_e(n) - W(n+k))^2, \tag{11}$$

$$\text{RMSE} = \sqrt{\frac{1}{N}\sum_{n=1}^{N} (N_e(n) - W(n))^2}. \tag{12}$$

2.5 Numerical free-decay tests and platform motions

The natural periods for heave and pitch of the platforms with CH, CHL, and CHS were calculated using WEC-Sim, incorporating platform hydrodynamic coefficients from previous NEMOH analyses. The heave natural period was determined by vertically displacing the structure and analysing the vertical oscillations, allowing the measurement of the platform's response to a vertical disturbance. Similarly, the pitch natural period was assessed by inclining the platform stern to observe the platform's rotational recovery around its lateral axis. The former natural periods were evaluated using the platform's catenary mooring line system, which was incorporated using Moordyn (Hall and Goupee 2015; Sirnivas et al. 2016). The natural periods of heave and pitch for the FOWT without CH are 17.5 s and 24.4 s, respectively (Bernal-Camacho et al. 2024). In addition, the platform model scaled at $\lambda = 1/340$ was used to determine its natural periods of heave and pitch, both without and with CH. These results were then converted to full-scale values using the Froude scaling law (Chakrabarti 1994), which means the model results were divided by $\sqrt{\lambda}$. The tests were conducted in a wave tank. A tracking mechanism was implemented to measure motions by placing white circular regions of interest (ROI), each with a diameter of 10 mm, on the platform's tower: one to measure heave and two to measure pitch. A high-speed camera, positioned 1.12 m from the platform with LED illumination, recorded its motion at 400 frames per second for 7.98 s, with a resolution of 656 pixels horizontally and 1024 pixels vertically. The captured images were analysed in ImageJ (Ferrerire and Rasb 2012) to track the centroids of the circular regions. Further details about the platform-scaled model, testing facility and measuring technique can be found in Bernal-Camacho et al. (2024), whilst the results are reported in Appendices 2 and 3.

The platform motions in surge, heave, and pitch were analysed under six different wave and wind conditions, without and with the motion reduction systems, to assess the effectiveness of varying centreboard and heave plate configurations in WEC-Sim. The motions were examined in detail after the platform experienced a backward surge drift induced by incoming wave and wind and reached its offset position. Once this equilibrium was attained, the platform exhibited cyclic behaviour, and the subsequent periodic translational and angular motions were analysed. To quantify the differences in motions between the FOWT without CH and the configurations with CH, CHL, and CHS, the normalised root-mean-square error (NRMSE), as defined in Eq. (13) was used. This metric incorporates the RMSE, previously described in Eq. (12). However, in this case, the sample size, initially represented by Ne and W in Eq. (11), is now adapted to compare the surge, heave, and pitch motions of the FOWT without CH against those of the FOWT with CH, CHL, and CHS. The denominator in Eq. (13) corresponds to the range (i.e., the difference between the maximum and minimum values) of the reference signal (R_s), representing the platform without CH

$$\text{NRMSE} = \frac{\text{RMSE}}{\max(R_s) - \min(R_s)}. \tag{13}$$

2.6 Limitations of the numerical study

The numerical model employed in this study involves some assumptions that define its scope and limitations. The hydrodynamic coefficients in NEMOH are computed using linear potential flow theory and assume an ideal fluid that is irrotational, inviscid, and incompressible. Consequently, nonlinear effects, such as viscous damping, vortex shedding, and flow separation resulting from the interaction between the fluid and the platform geometry, are neglected. The time-domain

simulations in WEC-Sim and MOST also assume rigid-body motion and linear hydrodynamics, with only three degrees of freedom: surge, heave, and pitch. These simplifications should be considered when interpreting the results, as they may influence the FOWT behaviour under real sea conditions. Nevertheless, this study provides an estimate of the platform's performance in regular wave conditions and under constant wind velocity.

3 Results and discussion

3.1 Sea conditions at sites A and B

The statistical analysis of wave conditions at the studied sites showed previously in Fig. 2 are summarised in the joint probability plot in Fig. 5a and Fig. 5b. The plots represent the relationship between Tp and Hs, with the average WV in m/s displayed within each cell. At site A, Fig. 5a, the predominant wave conditions are characterised by Tp values ranging from 2.25 to 7.75 s and Hs values between 0.22 and 4.25 m. This analysis identified three representative sea conditions (RSC) for numerical simulations under typical offshore scenarios, with probabilities of occurrence of 1.4%, 0.8%, and 0.4%, shown in Table 6 site A, from cases 1–3, and three extreme sea conditions (ESC) were selected to evaluate platform performance in harsh environments, as were cases 4–6, also listed in Table 6. For site B, Fig. 5b, the wave conditions show Tp values between 3.5 s and 9.25 s and Hs values from 0.25 m to 5.25 m. As summarised in Table 6 site B, three RSC, from cases 1–3, were chosen with probabilities of 1.07%, 0.4%, and 0.2%, along with three ESC, from cases 4–6.

3.2 Hydrodynamic properties of the platform configurations

The hydrodynamic coefficients of the platform configurations at site A and B were calculated using NEMOH, based on a mesh selection that resulted from a mesh dependency analysis conducted with three different mesh sizes: coarse, medium, and refined, and are discussed in this section. Although these coefficients primarily depend on the wetted surface geometry, they are also slightly influenced by water depth. Therefore, results for both sites are presented. Furthermore, the added mass coefficients for surge, heave, and pitch obtained from NEMOH were compared to those presented in Robertson et al. (2014) for the validation of potential flow theory, which utilised WAMIT. The details of the mesh dependency analysis, as well as the comparison of the added mass between NEMOH and WAMIT, can be found in Appendix 1.

3.2.1 Added mass coefficients

The added mass coefficients for surge, heave, and pitch in the frequency range from 0 to 0.8 Hz at site A are shown in Fig. 6a–c. In surge, presented in Fig. 6a, the platform without CH exhibits a lower added mass across the frequency range, with a peak value of 11.8E + 6 kg around 0.17 Hz. The CHS configuration presents higher added mass values, exceeding 12E + 6 kg at 0.17 Hz. In heave, as shown in Fig. 6b, the added mass without CH remains below 1.51E + 7 kg, whereas with CHS, it is above 1.8E + 7 kg across the entire frequency range. In pitch illustrated in Fig. 6c, the trend continues, with the platform without CH stabilising around 7.0E + 6 kg m^2 at higher frequencies, whilst the CHS configuration reaches up to 8.4E + 9 kg m^2 and stabilises at higher frequencies around 7.7E + 9 kg m^2. At site B, the added mass coefficients for surge, heave, and pitch, as illustrated in Fig. 6d–f, reveal differences amongst the four platform configurations. In surge, as depicted in Fig. 6d, the platform without CH exhibits the lowest added mass, reaching approximately 10.6E + 6 kg at the first peak, whereas the modified configurations exceed 12E + 6 kg. The added mass stabilises at frequencies above 0.3 Hz, with CHL maintaining the highest values and the configuration without CH consistently presenting the lowest. The CHS configuration yields a lower added mass than the CH and CHL cases, particularly in the high-frequency range. A similar trend is observed in the heave in Fig. 6e, where the platform without CH exhibits the lowest added mass, stabilising around 1.38E + 7 kg at higher frequencies. The introduction of the motion reduction system results in increased added mass, with the CHL configuration reaching the highest values, exceeding 1.9E + 7 kg. The CH and CHS configurations exhibit similar trends, with values of approximately 1.9E + 7 kg and 1.8E + 7 kg, respectively. In pitch, as displayed in Fig. 6f, the platform without CH configuration again exhibits the lowest added mass, stabilising near 7.0E + 9 kg m^2 at higher frequencies. The CHL configuration reaches its highest values, peaking above 9.5E + 9 kg m^2, indicating increased rotational inertia. The CH and CHS configurations fall between the former values, with CH presenting higher values than CHS. In general, the results demonstrate that the addition of the submerged centreboard and heave plate surfaces increases the added mass coefficients in all three degrees of freedom at sites A and B.

3.2.2 Radiation damping coefficients

The radiation damping coefficients in surge, heave and pitch for site A are presented in Fig. 7a–c. In surge, as shown in Fig. 7a, both configurations exhibit similar trends, with a dominant peak at approximately 0.18 Hz. The peak value is higher for the platform without CH, reaching approximately 6.7E + 6 N s/m, compared to about 6.6E + 6 N s/m with

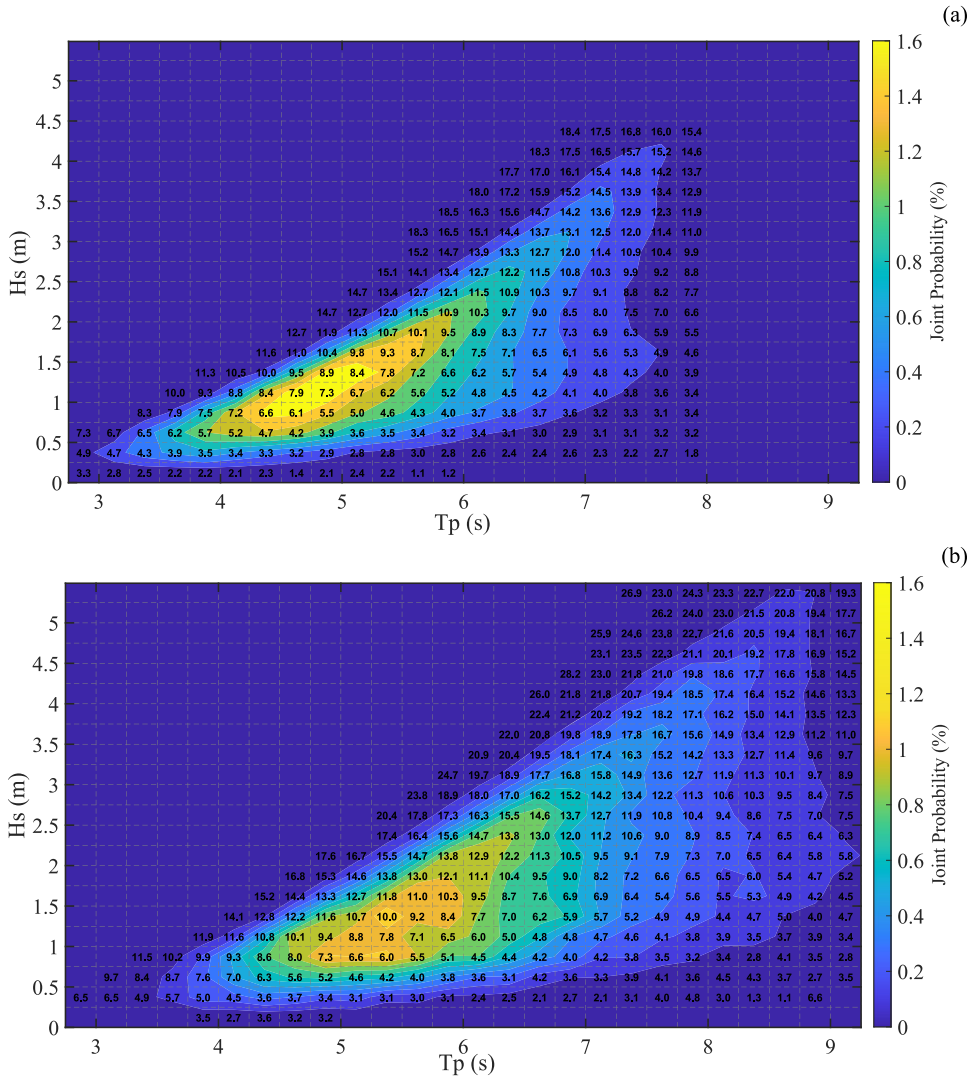

Fig. 5 The annual joint probability of Tp and Hs with the average WV in site A (**a**) and site B (**b**)

Table 6 RSC in cases 1–3 and ESC in cases 4–6 at sites A and B

Cases		Site A		
		Tp (s)	Hs (m)	WV (m/s)
RSC	1	5.5	1.75	9.3
	2	7	3	12
	3	7.5	4	15
ESC	4	11	9	21
	5	10	7.9	19
	6	9.5	7	18
			Site B	
RSC	1	5.5	1.5	10.5
	2	7.5	3.5	16.5
	3	8.5	4.5	19.2
ESC	4	12	9.6	24.5
	5	11	8.2	23
	6	10.6	7.1	21

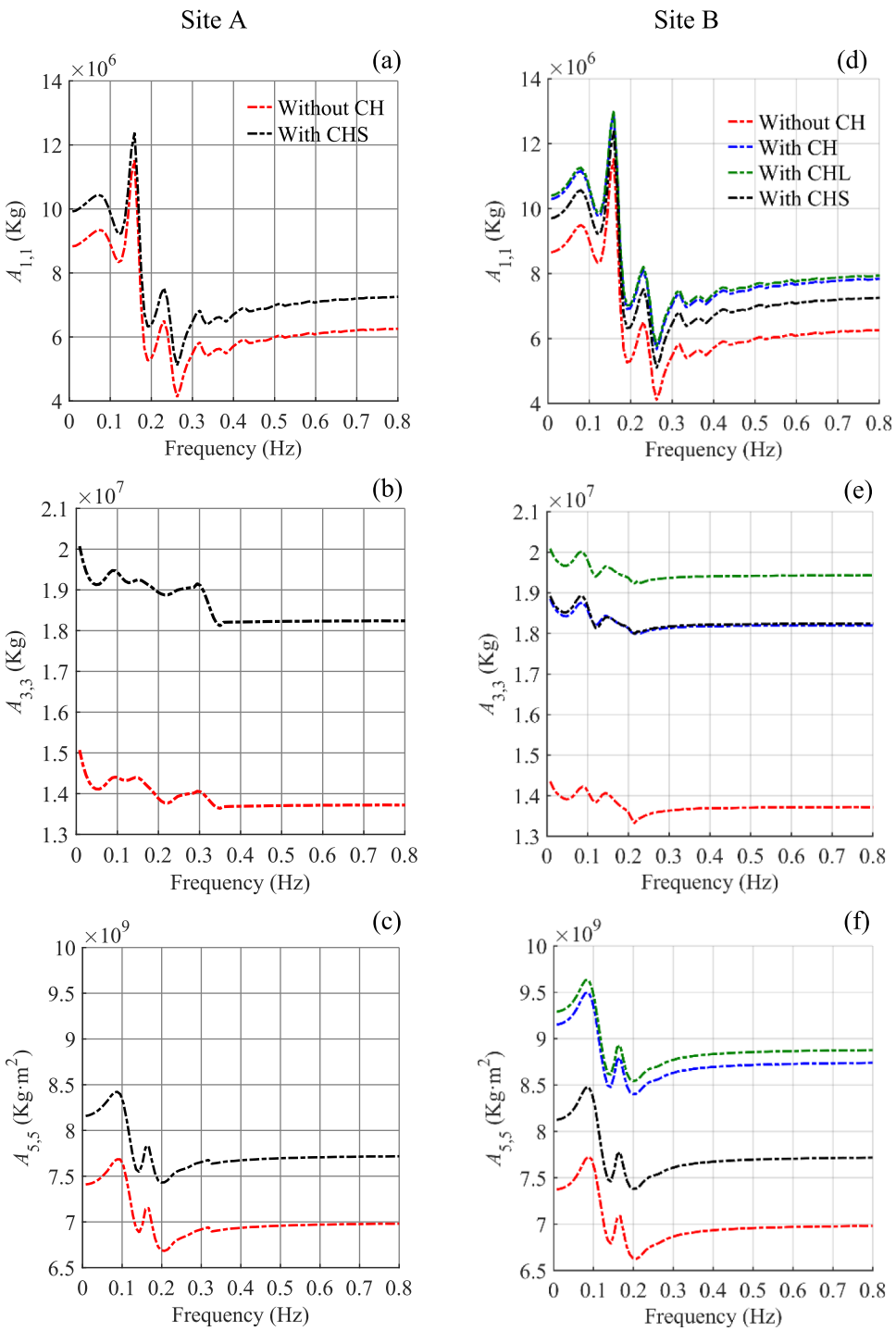

Fig. 6 Added mass coefficients for surge, heave, and pitch in **a–c** for site A, and **d–f** for site B

CH. Beyond 0.18 Hz, the damping has lower values with a decreasing tendency. Figure 7b shows the heave, where the configuration without CH exhibits a more pronounced damping peak, exceeding 6.2E + 5 N s/m at around 0.21 Hz. The CHS configuration shows a lower peak of 4.2E + 5 N s/m, featuring reduced radiated wave energy. For pitch illustrated in Fig. 7c, both configurations exhibit two peaks near 0.12 Hz and 0.18 Hz, with the platform without CH showing higher damping values, reaching up to 6.8E + 8 kg m^2/s. The CHS configuration shows slightly reduced peaks. After 0.3 Hz, values converge and stabilise near zero. Figure 7d–f depicts the radiation damping coefficients in site B. In surge, as presented in Fig. 7d, the four configurations exhibit similar damping behaviour, with a peak around 0.18 Hz, reaching values of approximately 6.5E + 6 Ns/m. After 0.18 Hz, the damping behaviour is like that of site A, decreasing until

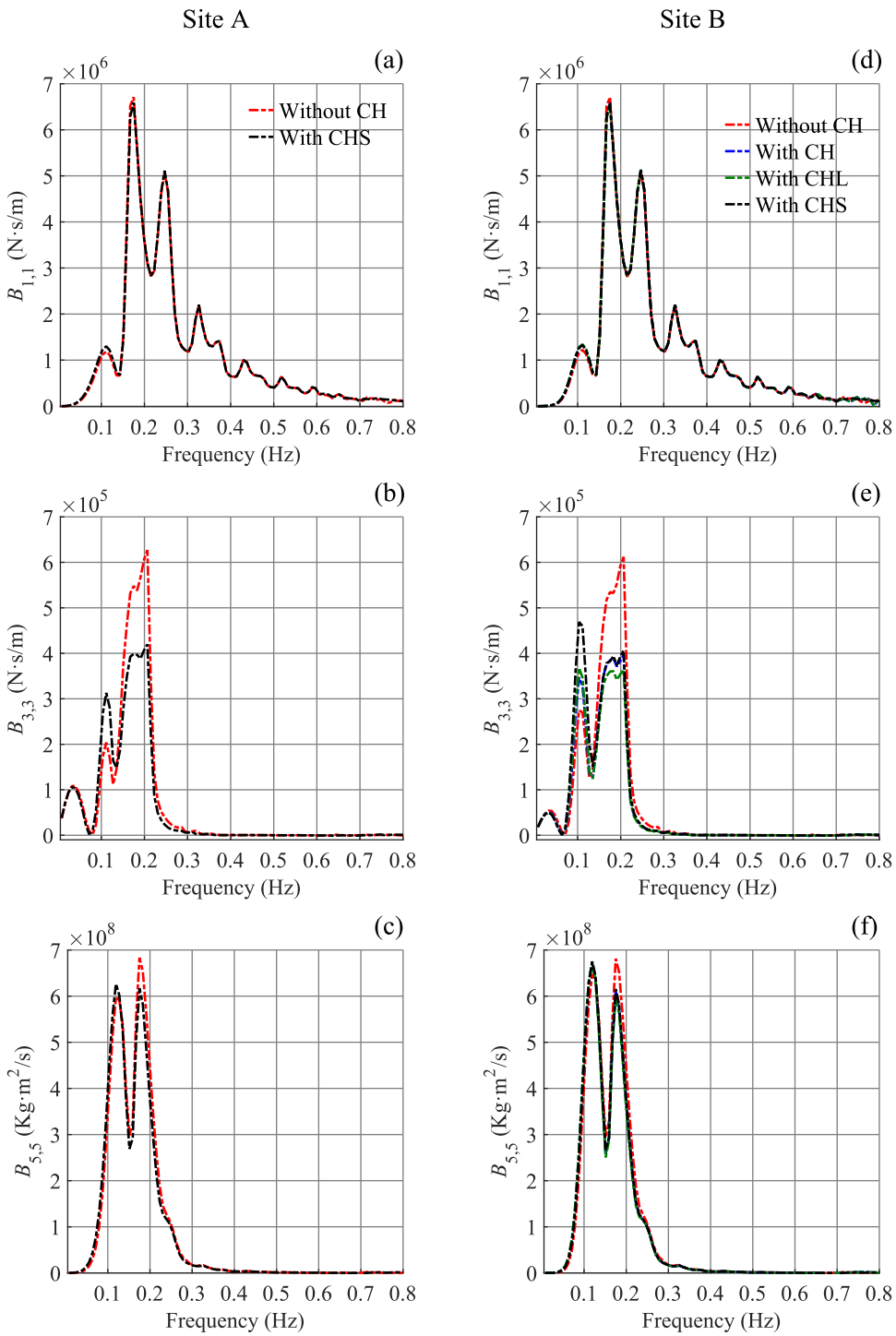

Fig. 7 Radiation damping coefficients for surge, heave, and pitch in **a**, **b** and **c** for site A, and **d**, **e** and **f** for site B

0.8 Hz. In heave, introducing the motion reduction system leads to notable variations in damping. The platform without CH exhibits the highest damping peak, exceeding 6.0E + 5 Ns/m around 0.2 Hz. At the same time, the CHL, CH, and CHS configurations display lower peaks. After 0.3 Hz, all configurations converge towards low-damping values. In pitch, the damping trends resemble those observed in heave, with two primary peaks at 0.12 Hz and 0.18 Hz, reaching values of approximately 6.5E + 8 kg m^2/s. The configuration without CH exhibits the highest damping peak. Beyond 0.3 Hz, all configurations experience a drop in damping, stabilising at near-zero values. Overall, the radiation damping results indicate that the submerged surface of the motion reduction system has a minor effect on the surge. However, it

affects the heave more significantly, with greater differences between the four platform configurations. In pitch, some differences appear mainly at lower frequencies.

3.2.3 Response amplitude operators

Figure 8a–c displays the RAOs for surge, heave, and pitch, ranging from 0.08 to 0.19 Hz, for the platform configuration at site A. In surge, as shown in Fig. 8a, the platform with CHS exhibits higher RAOs, starting near 0.62 m/m at 0.08 Hz and gradually decreasing, with a secondary peak around 0.17 Hz. In contrast, the platform without CH shows minimal response, remaining below 0.03 m/m throughout. A similar trend is observed in heave, as shown in Fig. 8b, where the CHS configuration reaches a peak of approximately 0.15 m/m at around 0.09 Hz, whilst the platform without CH remains under 0.02 m/m. However, in pitch RAOs, as presented in Fig. 8c, show the opposite behaviour. The platform without CH exhibits the highest response, exceeding 3.1°/m at the beginning and decreasing steadily. The CHS configuration shows the lowest pitch RAOs across the entire frequency range. The RAOs for surge, heave, and pitch, for the four platform configurations at site B, are illustrated in Fig. 8d–f. In surge, depicted in Fig. 8d, the CHS configuration exhibits the highest RAOs across the frequencies, as seen in site A, reaching approximately 0.57 m/m at the beginning. In contrast, the other configurations remain nearly unchanged and below 0.03 m/m. Similarly, the CHS platform in heave, as presented in Fig. 8e, shows the highest RAOs, exceeding 0.25 m/m at lower frequencies, whilst the remaining configurations display lower values, not surpassing 0.02 m/m. However, the CHS platform behaves differently in pitch RAOs, as displayed in Fig. 8f, exhibiting the lowest response throughout the frequency range. The platform without CH initially has the highest pitch RAOs, surpassing 3.2°/m, whilst the CH and CHL configurations present intermediate and close values. The variations observed in the RAOs from NEMOH are due to differences in added mass, radiation damping, and hydrodynamic coupling introduced by the motion-reduction systems, particularly in the 0.11–0.17 Hz frequency range. Within this range, the A_{11}, A_{33}, and A_{55} values increase due to the larger wetted surface area provided by the motion reduction system. However, the radiation damping behaviour differs, particularly in the CHS configuration, where the B_{11} and B_{33} values decrease slightly at around 0.15 Hz, and the B_{55} value increases. These trends may explain the RAO behaviour: reduced damping in surge and heave enhances motion amplitudes, whilst higher damping in pitch suppresses angular motion. Thus, the CHS configuration exhibits higher surge and heave RAOs and lower pitch RAOs than the other platforms. Natural frequency shifts also influence the RAOs of the other platforms in surge and heave towards 0.08 Hz, which amplifies resonance effects; similar behaviour was also reported by Weller and Gueydon (2012). The pitch RAOs were also lower for the CH and CHL configurations, indicating that modifying the underwater geometry reduces angular motion.

3.3 Effect of centreboard and heave plate on platforms' motion response

The installation of the motion reduction system influences platform stability and motion response. Thus, the natural periods in the heave and pitch motions of the platform with CH, CHL, and CHS, tested at sites A and B, were calculated through a free-decay test using WEC-Sim. Additionally, physical free-decay wave tank test results for the platform model without and with CH were obtained. Both the natural periods obtained from the wave tank tests and WEC-Sim simulations showed agreement. For the FOWT without the CH configuration, the heave natural period was 18.05 s experimentally and 17.5 s numerically, a difference of 3.05%, and the corresponding pitch natural periods were 25.23 s and 24.4 s, differing by 3.29%. For the FOWT with CH, the heave natural periods were 19.52 s in the experiments and 19.5 s in WEC-Sim (0.11% difference), whilst the pitch natural periods were 29.09 s and 27.8 s, with a 4.43% deviation. Further details of the numerical and physical free-decay procedure and results are provided in Appendix 2. A comparison between the WEC-Sim simulation and the experimental results from a testing campaign (Bernal-Camacho et al. 2024) was conducted. The experiments were performed under regular wave conditions with Tp between 9.5 and 12 s (0.5 s intervals), a Hs of 3.4 m, and a WV of 22 m/s, which were also used in the simulations. The numerically obtained surge, heave, and pitch motions showed RMSE values of 0.174, 0.247, and 0.263, respectively, when compared with the experiments. These results suggest that WEC-Sim may estimate platform motions and provide insights during the early stages of technology development. A detailed comparison, procedure, and discussion of uncertainties is provided in Appendix 3.

As the next step of the numerical simulation, Table 7 presents the NRMSE for surge, heave, and pitch motion values for the baseline platform without CH and with CHS, respectively, for the six simulated sea states at site A. The CHS generally reduced platform motions, particularly in RSC cases 1–3. The translational surge and heave motions decreased within ranges of − 0.095 to − 0.154 and − 0.095 to − 0.172, respectively, whilst the angular pitch motion showed a more pronounced reduction between − 0.235 and − 0.966. In cases 4–6 with CHS, the same trend persisted but with smaller magnitudes, as surge and heave reductions ranged from − 0.017 to − 0.021 and − 0.027 to − 0.143, respectively. In contrast, pitch motion had mixed behaviour,

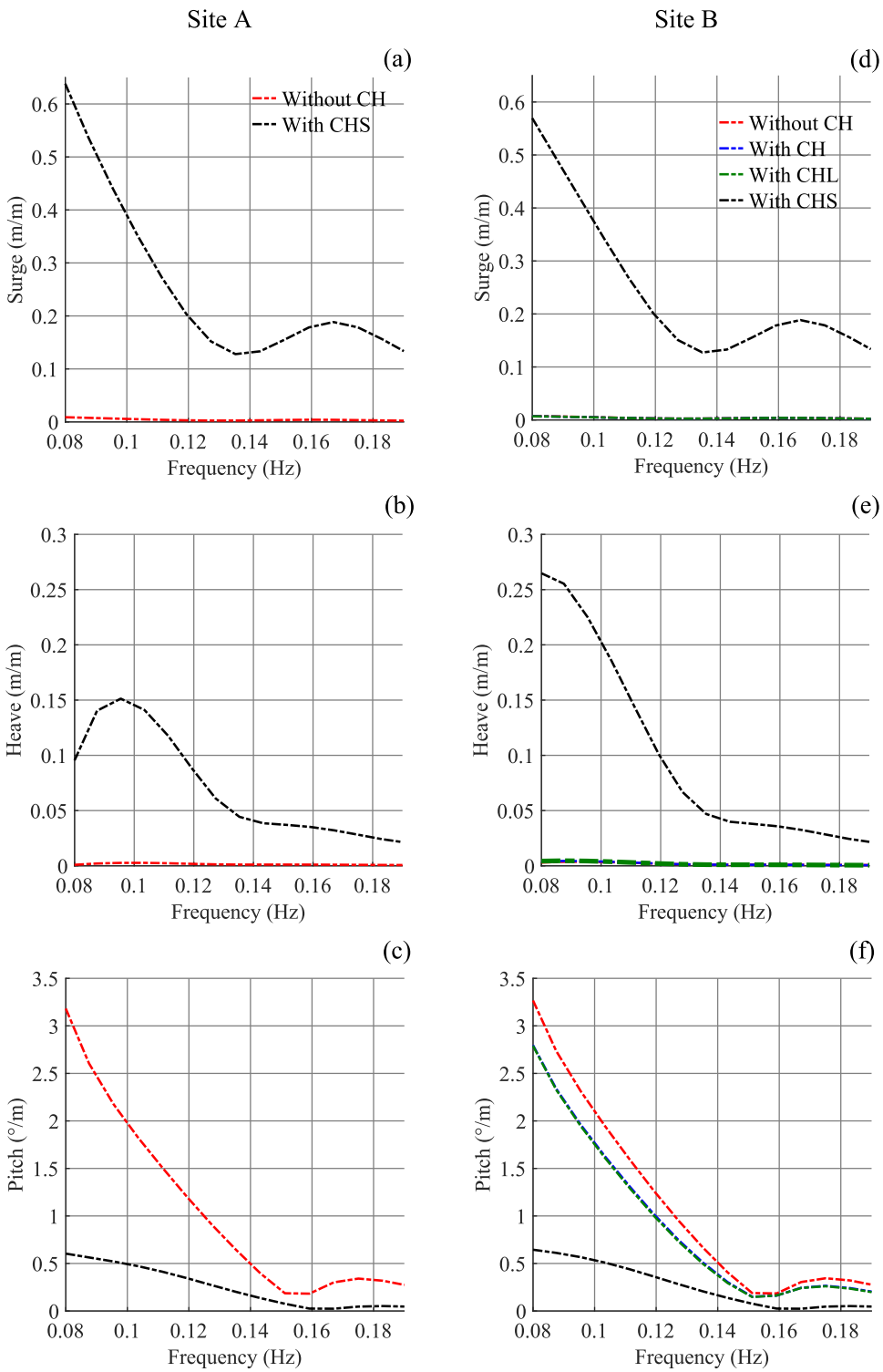

Fig. 8 RAOs for surge, heave and pitch without CH and with CH in **a–c** for site A, and without CH and with CH, CHL, and CHS in **d–f** for site B

Table 7 NRMSE between the platform without CH and with CHS in site A

Cases		CHS		
		Surge	Heave	Pitch
RSC	1	− 0.120	− 0.095	− 0.235
	2	− 0.095	− 0.172	− 0.966
	3	− 0.154	− 0.141	− 0.758
ESC	4	− 0.018	− 0.143	0.122
	5	− 0.021	− 0.036	− 0.159
	6	− 0.017	− 0.027	− 0.196

increasing by 0.122 in case 4 but decreasing by − 0.159 in case 5 and − 0.196 in case 6.

Amongst the most probable sea conditions, case 2 exhibited a significant decrease in motions. In extreme sea conditions, case 6 demonstrated a substantial reduction of motions, as indicated by the NRMSE values. Hence, Fig. 9 presents surge, heave, and pitch over time motion for cases 2 and 6. In case 2, the platform without CH exhibits an average surge oscillation between peak-to-trough of 0.415 m, which is reduced to 0.383 m with CHS. Similarly, the heave motion without CH oscillates by 0.150 m, decreasing to 0.110 m with CHS. In terms of pitch motion, the baseline platform oscillates by 0.309°, which is reduced to 0.283° with CHS. In case 6, the average peak-to-trough oscillation decreased from 2.580 to 2.456 m in surge, from 0.983 to 0.934 m in heave, and from 2.596° to 2.506° in pitch when comparing the configuration without CH to that with CH.

Table 8 compares the NRMSE values of surge, heave, and pitch motions between the baseline platform without CH and with CH, CHL, and CHS configurations at site B. It indicates that all configurations generally reduced platform motions at site B, with more pronounced effects under RSC than in ESC. In RSC, the three configurations consistently reduced platform motions across the three cases. The CHL configuration yielded the more significant reductions overall, with surge decreasing by up to − 0.672, heave by − 0.221, and pitch by − 0.878. The CH and CHS systems exhibited similar but slightly smaller reductions, with surge reductions ranging from − 0.596 to − 0.038 and pitch reductions between − 0.776 and − 0.331. Under ESC, the reduction magnitudes were smaller. For CH, surge, heave, and pitch decreased within − 0.030 to − 0.042, − 0.037 to − 0.101, and − 0.081 to − 0.133, respectively. CHL showed similar behaviour, with reductions ranging from − 0.032 to − 0.052 in surge, − 0.041 to − 0.099 in heave, and − 0.093 to − 0.152 in pitch. In contrast, CHS reduced surge by − 0.019 to − 0.061 but increased heave in all cases up to 0.095 and increased pitch in case 4 by 0.081 but decreased in the last two cases up to − 0.133. These results indicate that all configurations improve platform motion under RSC, though their effectiveness, particularly for CHS, is less under ESC, where motion increments may occur.

To illustrate the platform's motion under the most probable and extreme sea conditions at site B, cases 3 and 4 were selected, as they represent the highest Hs and wind velocity WV within their respective categories. Figure 10 presents the time-domain motions in surge, heave, and pitch for these cases. In case 3, the platform without CH exhibits a surge oscillation of 1.077 m, which is reduced to 0.980 m with CH, 0.971 m with CHL, and to 1.014 m with CHS. The heave motion decreases from 0.470 to 0.403 m and 0.391 m with CH and CHL, respectively, whilst CHS shows an increase to 0.481 m. The pitch oscillation is also reduced from 1.386° without CH to 1.194° with CH, 1.176° with CHL, and 1.305° with CHS. In case 4, the platform without CH surge motion, which is 5.576 m, is reduced to 5.191 m, 5.156 m, and 5.316 m with CH, CHL, and CHS, respectively. The heave motion decreases from 2.281 m without CH to 2.135 m with CH and 2.117 m with CHL, whilst CHS shows a higher value of 2.469 m. The pitch motion also reduces from 4.735° without CH to 4.442° with CH and 4.452° with CHL; however, it increases to 4.810° with CHS.

Across all sea conditions at sites A and B, a consistent reduction in surge motion was observed with the use of the centreboard and heave plate configurations. In the heave motion, the CHS configuration reduced the motion in all cases at site A. However, at site B, CHS did not reduce heave motion in four cases, whilst CH and CHL consistently improved performance. The most notable improvement was observed in pitch motion, where all three configurations limited the backwards tilt of the platform.

To provide additional insight into the platform motions evaluated through NRMSE, Appendix 4 includes Tables 16 and 17 presenting the mean peak-to-trough distances in surge, heave, and pitch motions, along with the maximum pitch tilt backwards for each configuration. These values are presented for the six sea conditions at sites A and B. These data support the NRMSE findings by showing the amplitude

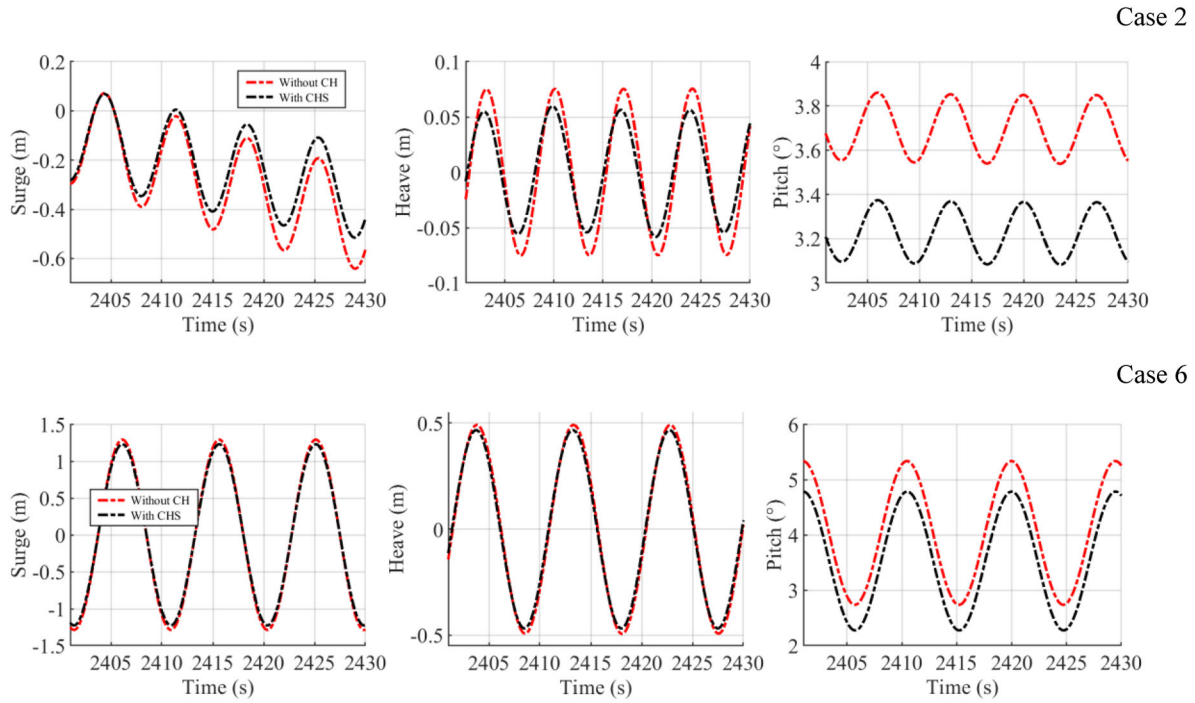

Fig. 9 Surge, heave, and pitch motions of the platform without CH and with CHS over time for cases 2 and 6

Table 8 NRMSE between the platforms without CH and with CH, CHL, and CHS configurations in site B under RSC and ESC

		CH CHL CHS								
		Surge	Heave	Pitch	Surge	Heave	Pitch	Surge	Heave	Pitch
RSC	1	− 0.596	− 0.099	− 0.473	− 0.672	− 0.119	− 0.542	− 0.595	− 0.094	− 0.479
	2	− 0.342	− 0.199	− 0.770	− 0.385	− 0.221	− 0.878	− 0.313	− 0.133	− 0.776
	3	− 0.042	− 0.051	− 0.331	− 0.049	− 0.059	− 0.378	− 0.038	0.039	− 0.332
ESC	4	− 0.034	− 0.101	− 0.081	− 0.044	− 0.099	− 0.093	− 0.058	0.095	0.081
	5	− 0.042	− 0.038	− 0.104	− 0.052	− 0.041	− 0.118	− 0.061	0.026	− 0.103
	6	− 0.030	− 0.037	− 0.133	− 0.032	− 0.043	− 0.152	− 0.019	0.016	− 0.133

of motions experienced by the platforms and the pitch motion reduction achieved by each configuration.

3.4 Structural loads

3.4.1 Mooring system forces and direction

Table 9 presents the resultant force of the mooring line and its direction acting on the platform without CH and with CHS at site A for the sea conditions simulated. In all cases, implementing the CHS increased the resultant force. Under RSC, installing the CHS configuration increased the resultant mooring force by approximately 1.05% across cases 1–3. In ESC, a minor increase of about 0.63% was observed in cases 4–6. The direction of the resultant mooring force vector exhibited minimal variation in all cases, with angular deviations below 1°

The resultant mooring forces and directions of the platforms at site B are summarised in Table 10. Under RSC, installing the CH, CHL, and CHS configurations led to consistent increases in the resultant mooring force of approximately 1.15%, 1.30%, and 1.16%, respectively, across cases 1–3. Similarly, with ESC, average increases of 1.19%, 1.35%, and 1.07% were observed for CH, CHL, and CHS, respectively. The direction of the resultant force varied by less than 0.35° in all cases. The increase in mooring force may be due to the additional weight of the motion-reduction system attached to the platform.

Although the centreboard and heave plate configurations reduced platform motions, an increase in the resultant mooring force was observed, suggesting that the motion reduction

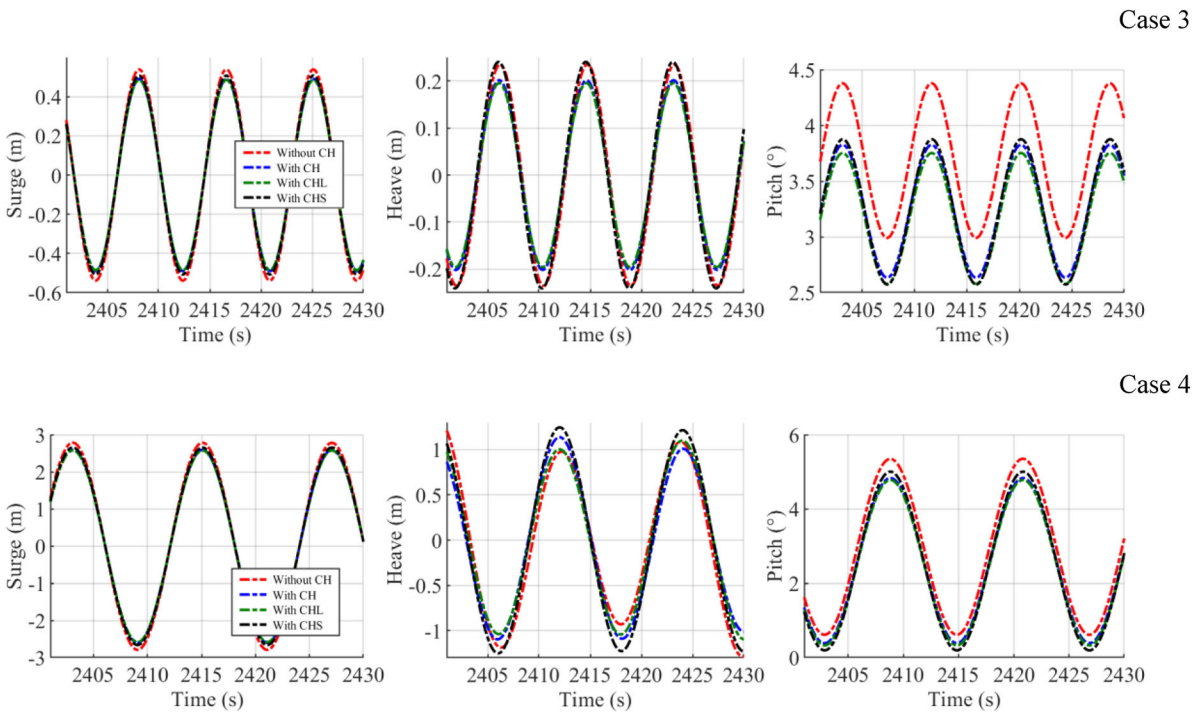

Fig. 10 Surge, heave, and pitch motions of the platform without CH and with CH, CHL, and CHS over time for cases 3 and 4

Table 9 Resultant force and direction of the mooring line system acting on the platform without CH and with CHS in site A under RSC and ESC

Cases		Resultant force (kN)	
		Without CH	CHS
RSC	1	543.124 ∠ 35.843°	546.750 ∠ 36.227°
	2	535.056 ∠ 35.496°	540.278 ∠ 36.415°
	3	559.321 ∠ 33.702°	567.643 ∠ 34.632°
ESC	4	533.672 ∠ 39.943°	535.180 ∠ 40.393°
	5	551.895 ∠ 37.062°	555.773 ∠ 37.613°
	6	556.670 ∠ 35.878°	561.727 ∠ 36.396°

Table 10 Resultant force and direction of the mooring line system acting on the platform without CH and with CH, CHL, and CHS in site B under RSC and ESC

Cases		Resultant force (kN)			
		Without CH	CH	CHL	CHS
RSC	1	953.007 ∠ 63.801°	963.594 ∠ 64.031°	965.057 ∠ 64.062°	963.741 ∠ 64.034°
	2	985.937 ∠ 61.779°	997.537 ∠ 62.036°	999.077 ∠ 62.06°	997.615 ∠ 62.039°
	3	969.689 ∠ 62.627°	981.019 ∠ 62.886°	982.537 ∠ 62.921°	980.979 ∠ 62.889°
ESC	4	913.935 ∠ 65.624°	924.178 ∠ 65.830°	925.664 ∠ 65.864°	922.662 ∠ 65.830°
	5	926.544 ∠ 64.884°	938.005 ∠ 65.149°	939.488 ∠ 65.189°	936.865 ∠ 65.165°
	6	945.213 ∠ 63.734°	956.799 ∠ 64.021°	958.282 ∠ 64.062°	955.866 ∠ 64.038°

system could affect design tolerances and long-term durability (Huang et al. 2024; Lian et al. 2023). Nevertheless, despite the higher mooring tension, benefits were achieved in structural load reduction and power output, as discussed in the following sections.

3.4.2 Tower base and blade root loads

Despite the increase in the resultant mooring line forces observed when the motion reduction systems were implemented, the tower base bending moment (My) decreased consistently across all sea conditions at both sites, as shown in Table 11. At site A, the CHS configuration reduced My compared to the platform without CH. Under RSC, cases 1–3, My decreased to 2.867–3.201 MN m, corresponding to a reduction of approximately 6.15%. Under ESC, cases 4–6, a similar reduction trend was observed, with values ranging from 3.072 to 3.096 MN m and an average decrease of about 6.42%, demonstrating the effectiveness of the CHS in mitigating tower loads. At site B, all three motion-reduction configurations, CH, CHL, and CHS, achieved decreases in My relative to the baseline platform. For RSC cases 1–3, the reduction ranged from 2.5–3.3 MN m ($\approx$ 6.15%), whilst for ESC cases 4–6, it varied between 2.3–3.0 MN m ($\approx$ 6.45%).

Another reduction trend was observed in the blade root moment My in some cases, although some increments were also identified. Table 12 presents the corresponding values for both sites. At Site A, under RSC, cases 1 and 2 showed reductions of 0.11% and 0.23%, respectively, whilst case 3 exhibited an increase of 2.14%. In ESC, increases were observed in cases 5 and 6 ($\approx$ 0.09%), whereas case 4 showed a reduction of 0.43%. At Site B, during RSC, cases 2 and 3 showed increases in My of about 0.09% on average for CH, CHL, and CHS. In contrast, case 1 displayed reductions of 0.15%, 0.18%, and 0.17% for CH, CHL, and CHS, respectively. Under ESC, a consistent reduction trend was observed in cases 4–6, with average decreases of 0.21% for CH, 0.26% for CHL, and 0.37% for CHS.

The motion reduction system demonstrated greater and more consistent reductions in tower base loads compared to those at the blade root across all six cases. These reductions are attributed to the stabilisation of platform motions provided by the CH, CHL, and CHS configurations. Although mooring line forces were not reduced as seen previously, the centreboard and heave plate system dampened platform motions, leading to lower structural loads, which may prolong the lifespan of the FOWT.

3.5 Rotor power output, torque and pitch controls analysis

The rotor exhibited distinct control responses in the sea conditions at both sites. At site A, case 1 involved only torque control, with torques of 21.550 kN m without CH, and 21.657 kN m with CHS. In case 2, although the wind speed of 12 m/s exceeded the rated value of 11.4 m/s, torque control remained active alongside a blade pitch of 5.897°, resulting in torques of 29.453 kN m without CH, and 29.575 kN m with CHS. This is attributed to platform-induced variations in relative wind speed across the blade sections. From case 3 onward, torque control reached its rated value of 43.093 kN m, and the system transitioned to pitch control. At site B, only case 1 showed non-rated torque values of 25.134 kN m, 25.206 kN m, 25.216 kN m, and 25.155 kN m for the platform without CH, with CH, CHL, and CHS, respectively, where torque control was acting alone. In all other cases, torque remained at 43.093 kN m.

Table 13 shows the mean power output and blade pitch across the configurations at both sites. At site A, the CHS configuration resulted in a slight increase in power output in cases 1–3 (RSC) by 0.67%, 0.52%, and 0.45%, respectively. Under ESC, in case 4 the power output remained constant at 5 MW but increased by 0.26% and 0.29% in cases 5 and 6, respectively, with CHS. Blade pitch at site A ranged from 5.897° to 16.306° in cases 2–6, with no blade pitch in case 1. At site B, the addition of the CH, CHL, and CHS resulted in slight increases in power output across all cases. The highest

Table 11 The tower base bending moment across six sea conditions for different platform configurations at sites A and B under RSC and ESC

		Tower base My (MN m)					
		Site A		Site B			
		Without CH	CHS	Without CH	CH	CHL	CHS
RSC	1	48.411	45.544	44.729	42.217	41.849	42.186
	2	48.373	45.481	51.772	48.871	48.466	48.844
	3	53.278	50.077	48.787	46.022	45.629	45.990
ESC	4	46.316	43.244	39.048	36.723	36.361	36.587
	5	50.419	47.373	41.129	38.726	38.354	38.578
	6	51.810	48.714	44.840	42.221	41.830	42.097

Table 12 Blade root bending moment across six sea conditions for the platform configurations at sites A and B under RSC and ESC

		Blade root My (MN m)					
		Site A		Site B			
		Without CH	CHS	Without CH	CH	CHL	CHS
RSC	1	9.376	9.366	9.208	9.194	9.191	9.192
	2	9.867	9.844	10.660	10.672	10.673	10.673
	3	9.633	9.843	11.381	11.386	11.385	11.387
ESC	4	11.045	10.998	10.268	10.242	10.237	10.227
	5	11.365	11.376	10.564	10.542	10.537	10.526
	6	11.205	11.216	11.013	10.994	10.988	10.974

Table 13 Mean power output and blade pitch angle for different FOWT configurations at sites A and B under RSC and ESC

Cases		Power output (MW)							
		Site A			Site B				
		Without CH	CHS	Blade pitch (°)	Without CH	CH	CHL	CHS	Blade pitch (°)
RSC	1	1.927	1.940	0	2.295	2.302	2.303	2.302	3.500
	2	2.880	2.895	5.897	4.486	4.500	4.502	4.500	11.186
	3	4.002	4.020	9.492	4.941	4.950	4.952	4.950	14.106
ESC	4	5.000	5.000	16.306	5.000	5.000	5.000	5.000	20.310
	5	4.920	4.933	13.894	4.996	4.998	4.998	4.998	18.658
	6	4.786	4.800	12.825	4.987	4.989	4.989	4.989	16.327

gains during RSC occurred in case 2, with increases of 0.31% with CH, 0.36% with CHL, and 0.31% with CHS. In ESC, the output remained at 5 MW in case 4 and increased by 0.05% in cases 5 and 6. Blade pitch angles at site B ranged from 3.5° to 20.310°.

4 Conclusion

The present study evaluated the performance of the OC4 DeepCwind FOWT, equipped with a motion reduction system comprising a rectangular centreboard and a circular heave plate installed on the central column. A series of simulations were conducted to ascertain the effects of regular wave conditions and constant wind flow on the sea. The simulations utilised sea conditions from two North Sea sites within the EEZs of the Netherlands and the United Kingdom. The key findings include:

- At Site A, the CHS configuration successfully mitigated surge and heave motions in all six cases, whilst also achieving this reduction in five out of six cases for pitch motion. At Site B, where CH, CHL, and CHS configurations were tested, it was found that CHL achieved the most significant reduction in surge, heave, and pitch motions across all sea conditions, followed by CH. In contrast, CHS showed limited effectiveness at Site B, manifesting as increased heave in five cases and increased pitch in a single case.
- The incorporation of the motion reduction system CH, CHL, or CHS resulted in increased mooring line forces at both locations. However, a reduction in the tower base My was observed across all configurations, and the blade root My decreased in three cases at Site A and four at Site B.
- The hypothesis that the power output would be enhanced by reducing the platform motions was confirmed by the numerical simulations, which showed a slight improvement in power output at both sites when the motion reduction configurations were employed.

The motion analysis revealed that the most notable improvement was a reduction in pitch, particularly in limiting the platform's backwards tilt. The implementation of motion reduction systems has been demonstrated to result in a mean reduction in NRMSE pitch of − 0.366 (as shown in Tables 7, 8). This reduction contributed to a decrease in the My loads at the tower base and blade root. These results

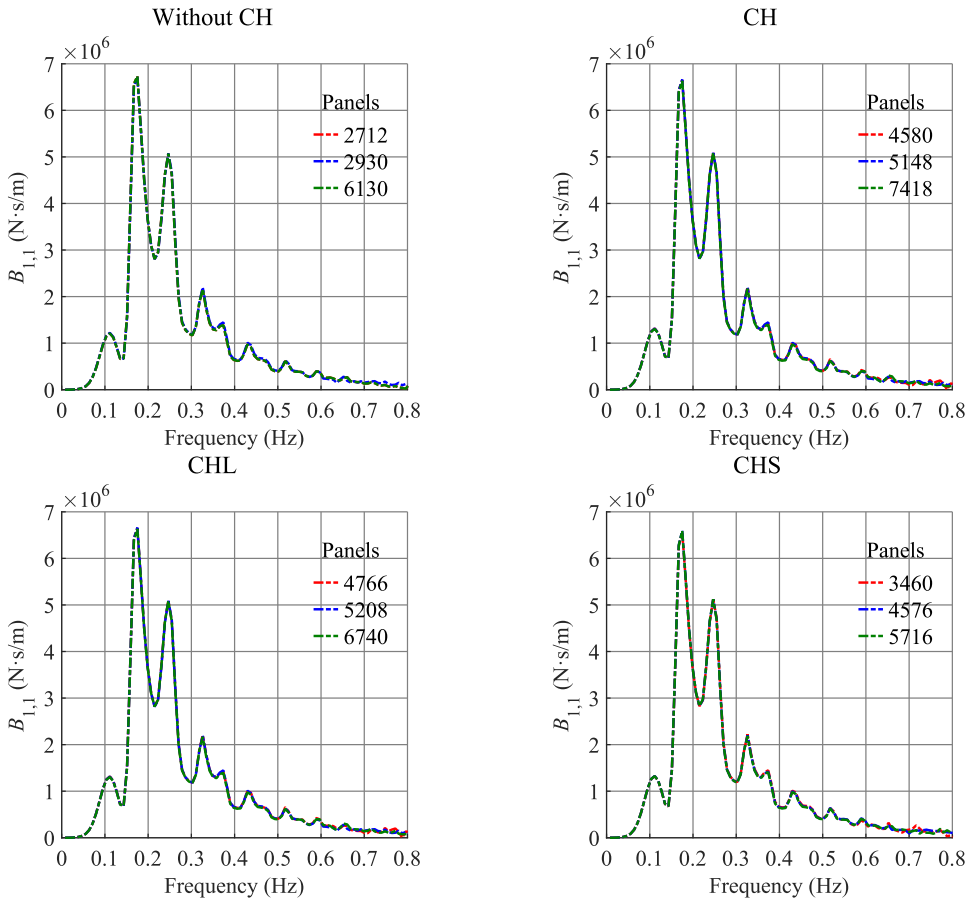

Fig. 11 Mesh convergence analysis of the platform without CH and with CH, CHL, and CHS. The plots represent the surge radiation damping in the wave frequency domain of each platform configuration

indicate that the proposed centreboard and heave plate configurations can help mitigate fatigue loads and extend the platform's operational lifespan. Future work should focus on optimising the system design and evaluating its performance across various platform types, sea conditions, and including all six degrees of freedom under different wave directions, irregular waves, and turbulent wind. Moreover, proper scale model experiments or high-fidelity CFD simulations are recommended to assess the passive motion-reduction system configurations under nonlinear hydrodynamic effects.

Appendix 1: Mesh dependency analysis and comparison of FOWT added mass coefficients results from NEMOH and WAMIT using cross-correlation and root mean square

The platform's wetted surface was discretised using three different mesh configurations to verify the convergence of the results. For the FOWT without CH, the analysis began with a mesh comprising 2712 panels, followed by a second mesh with 2930 panels and a finer mesh with 6130 panels. The surge radiation damping ($B_{1,1}$) results, as shown in Fig. 11, indicate that the second mesh with 2930 panels differed by less than 0.6% from the initial and finer meshes. As a result, the 2930 panel mesh was selected for subsequent simulations. Similarly, for the FOWT with CH, three mesh configurations with 4580, 5148, and 7418 panels were tested. The second mesh, consisting of 5148 panels, was chosen as it exhibited a deviation of less than 0.7% compared to the coarser and finer meshes. The FOWT with CHL mesh configurations included 4766, 5208, and 6740 panels. The second configuration, with 5208 panels, was selected, because it showed a variation of 2.9% compared to the coarser mesh and 2.8% compared to the finest mesh. The last FOWT with CHS configuration was analysed using 3460, 4576, and 5716 panels mesh resolutions. The mesh with 4576 panels was selected, as it exhibited a difference of less than 1.2% compared to the coarser and finer meshes. The second mesh was chosen in all cases, as it provided a good balance between computational time and results for both the coarser and finer meshes.

The hydrodynamic coefficients calculated in WAMIT for the OC4 DeepCwind platform, as reported in Robertson et al. (2014) and used for model validation, are compared with the results obtained in this study. The value of R was computed for the FOWT for the surge ($A_{1,1}$), heave ($A_{3,3}$), and pitch ($A_{5,5}$) added mass from NEMOH and WAMIT results, which

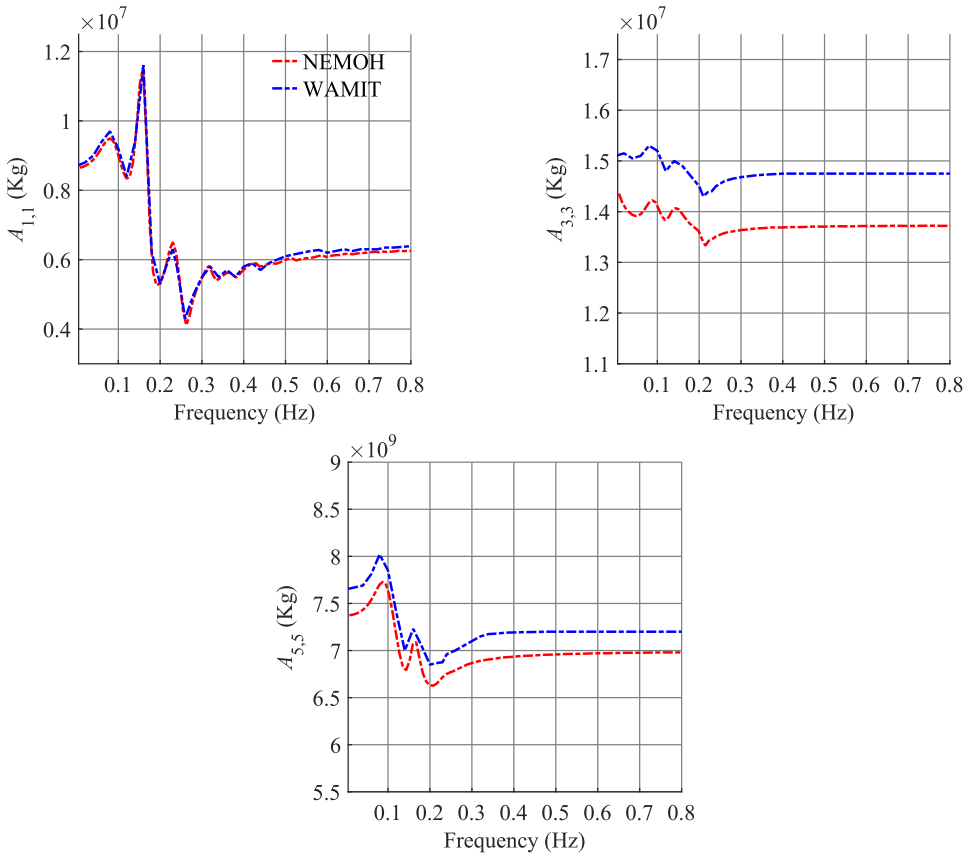

Fig. 12 Comparison of the surge, heave, and pitch-added mass results from NEMOH and WAMIT (Robertson et al. 2014) for the OC4 DeepCwind semi-submersible platform

are depicted in Fig. 12. The highest value of R occurred at $k = 0$ in the three cases, indicating synchronised signals. The RMSE calculation has values of 0.02, 0.11, and 0.25 for surge, heave, and pitch, respectively.

The discrepancies in the hydrodynamic coefficients calculated by NEMOH compared to those reported in WAMIT arise from differences in the numerical setups. For instance, the braces were excluded in the NEMOH simulations to minimise the number of panels required, thereby reducing computational time. Additionally, the mesh resolution used to discretise the platform surface in this work differs from that used in WAMIT, and the frequency step is also different.

Appendix 2: Heave and pitch free-decay results: numerical and experimental comparison

Figure 13 presents the heave and pitch free-decay test results for the FOWT with the CH configuration. The same procedure was applied to the CHL and CHS configurations, showing similar signal response patterns. Thus, only the CH configuration is displayed to avoid redundancy, as differences are limited to the natural heave and pitch periods between signal peaks. The introduction of the motion reduction system increases the platform's natural periods. The natural heave period extends from 17.5 s without CH to 19.5 s with CH, whilst the pitch natural period increases from 24.4 s to 27.8 s. The CHL configuration exhibits natural periods of 20 s for heave and 28.1 s for pitch, whereas the CHS configuration yields natural periods of 19.2 s for heave and 27 s for pitch. The four configurations maintain natural periods that extend beyond the typical ocean wave period range of 3–17 s (Holthuijsen 2010), making them suitable for operation under these conditions.

On the other hand, the tests in the wave tank involved applying initial displacements to the platform in the heave and pitch directions. For the platform without CH, an initial heave displacement of 60 mm was applied, whilst for the platform with CH, the displacement was 60.6 mm. Similarly, initial pitch angles of 23° and 29° were applied for the platforms without and with CH, respectively. Although the initial heave displacement and pitch inclination differ, these variations are not expected to affect the natural period results, as the natural period depends on the platform's physical properties and should remain constant regardless of initial conditions, provided that the water remains calm. The motion data were recorded and plotted, with time on the x-axis and

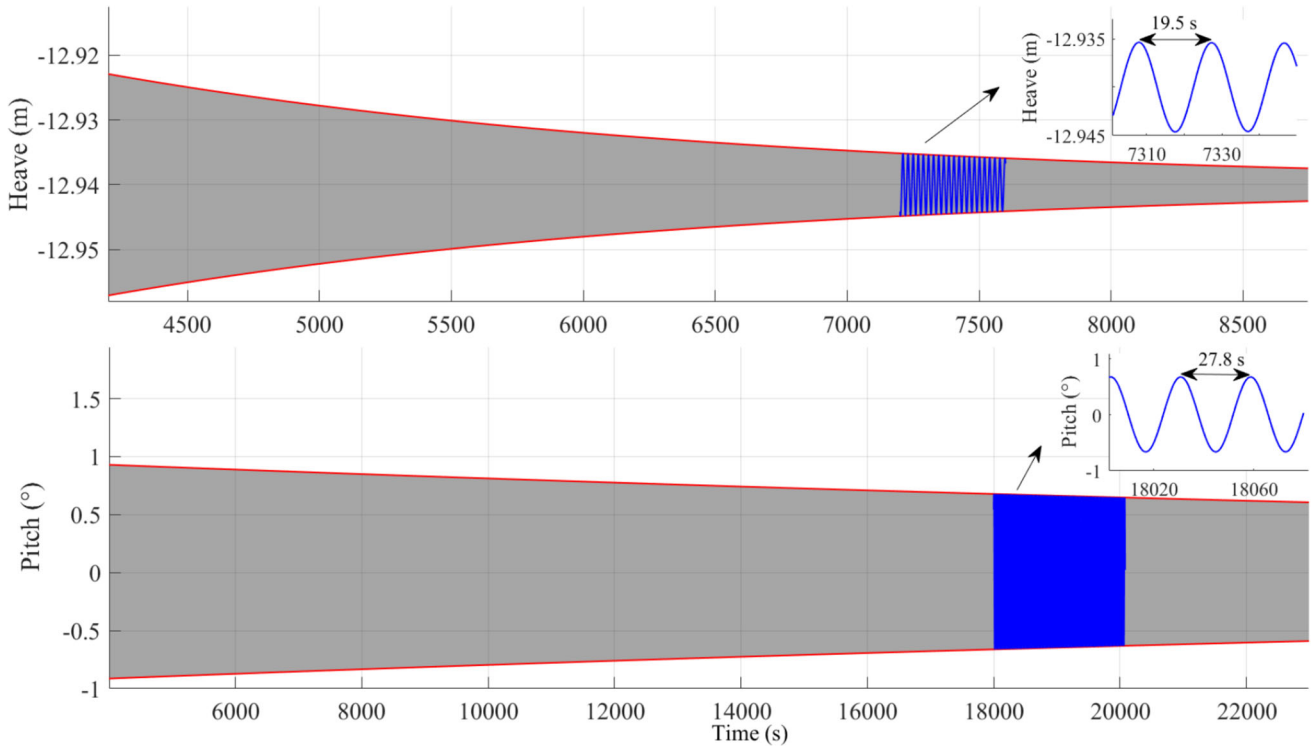

Fig. 13 The natural period in heave and pitch of the platform with CH

heave (mm) and pitch (°) motions on the *y*-axis. The platform's natural periods were determined by analysing the time intervals between successive peaks in the recorded signals. Figure 14 presents the initial set-up of the heave-free decay test, the maximum submergence of the platform following its release, and final frames to illustrate various stages of the testing procedure for the FOWT without and with CH. This figure also highlights the holding line attached to the central column (CC), the ROI, the initial upward heave displacement distance, and the water line (WL). Likewise, Fig. 15 provides similar information for the pitch-free decay test at both platform configurations, including the platform's initial backwards pitch angle.

The results of the free decay test signal across the time-domain in heave and pitch, without and with CH, are presented in Fig. 16. These indicate that the platform's natural periods increased with the inclusion of the CH, rising from 0.98 to 1.06 s for heave and from 1.37 to 1.58 s for pitch. Table 14 presents the full-scale heave and pitch natural periods of the platform, both without and with CH, obtained from physical tests and WEC-Sim simulations, along with the percentage differences between them.

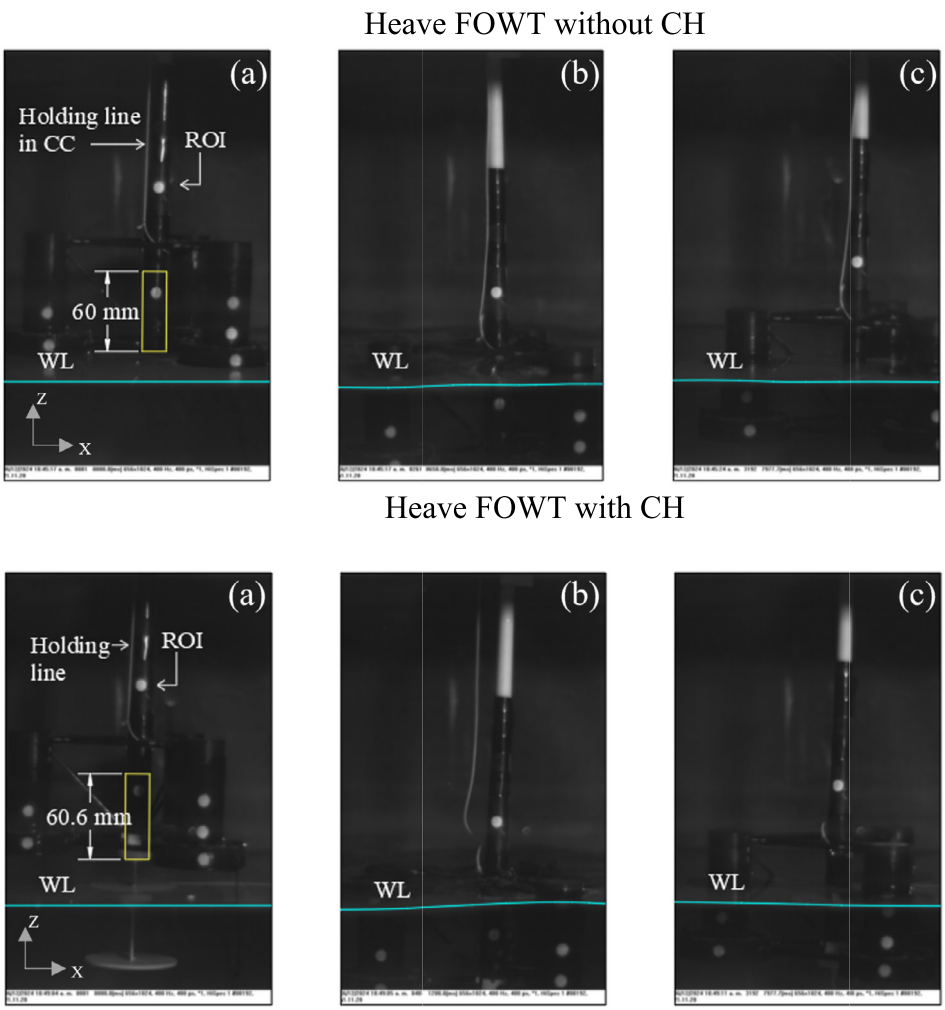

Fig. 14 Initial **a**, maximum submergence **b** and final frames **c** of the FOWT without and with CH in the heave-free decay test

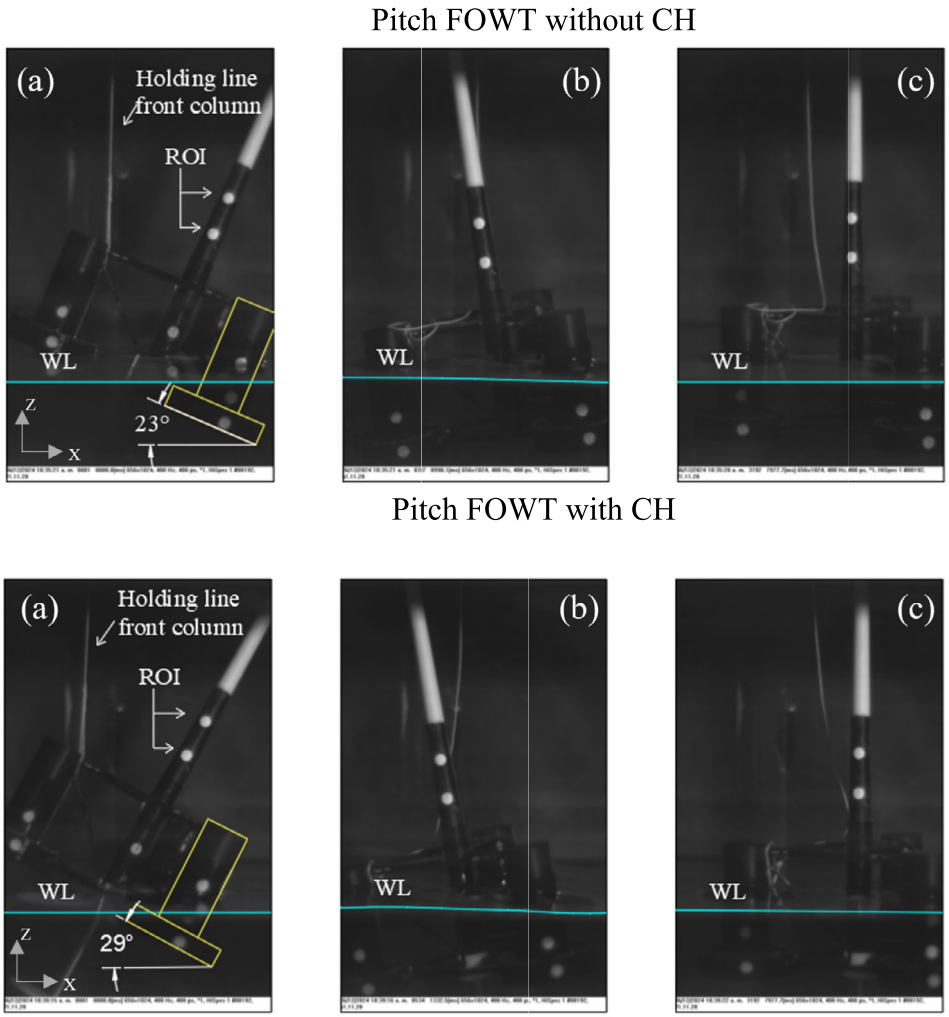

Fig. 15 Initial **a**, maximum post-release pitch **b**, and final frames **c** of the FOWT without and with CH in the pitch-free decay test

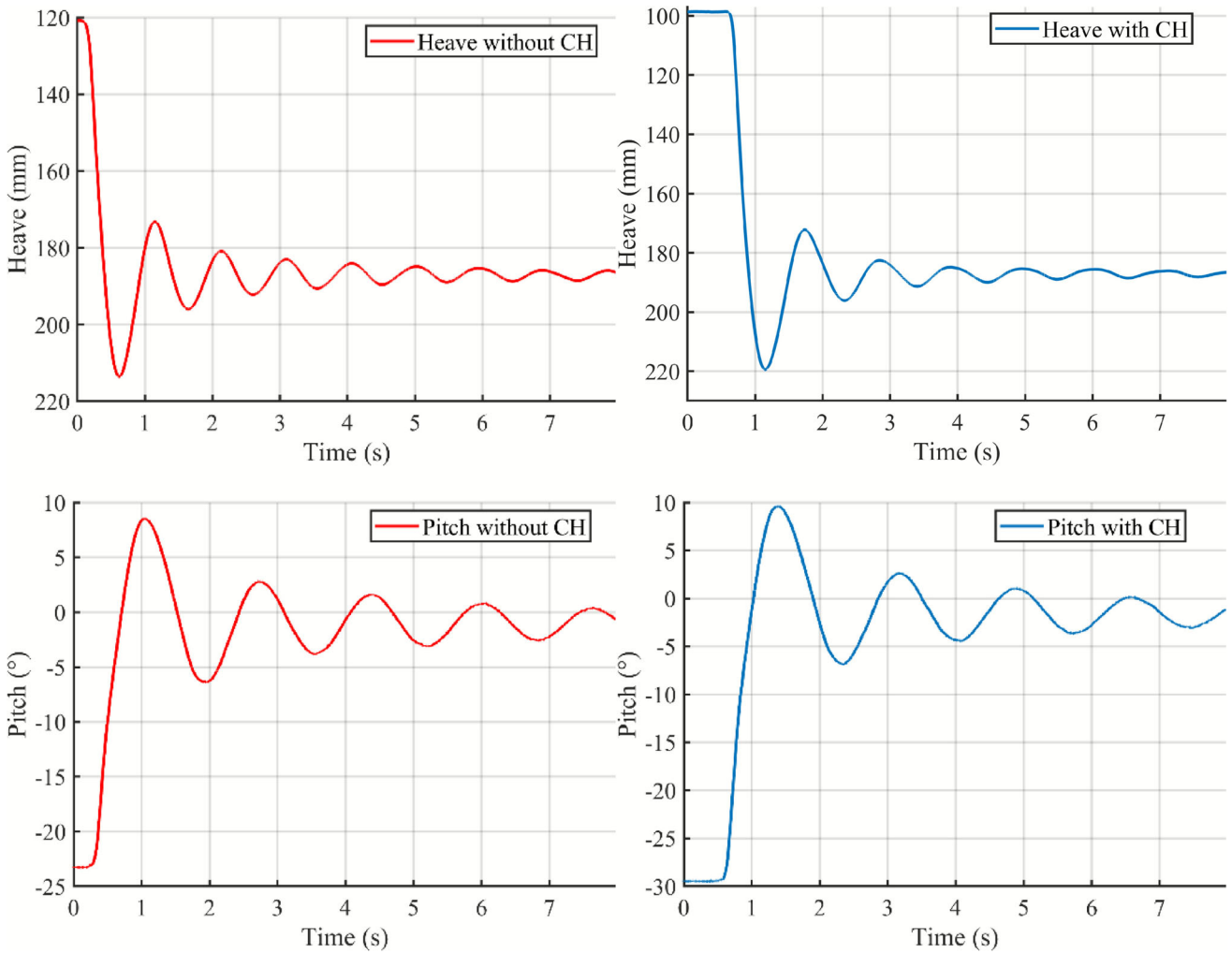

Fig. 16 FOWT without and with CH heave and pitch-free decay test signal

Table 14 Heave and pitch motion natural periods for the baseline platform without and with CH in the test and WEC-Sim at full scale, along with the difference in percent

Motions	FOWT	Results		Difference (%)
		Test	WEC-Sim	
Heave	Baseline	18.05	17.5	3.05
	CH	19.52	19.5	0.11
Pitch	Baseline	25.23	24.4	3.29
	CH	29.09	27.8	4.43

Appendix 3: Comparison of WEC-Sim and experimental results for surge, heave, and pitch motions of the FOWT without and with CH

The FOWT results, without and with CH, from WEC-Sim, were compared to those obtained in an experimental testing campaign (Bernal-Camacho et al. 2024) conducted in an enclosed wave-wind flume (WWF). The sea conditions used in the experiment and for comparison were regular waves with wind (RWW), characterised by Hs of 3.4 m, WV of 22 m/s, and a Tp varying from 9.5 to 12 s at 0.5 s intervals, resulting in six distinct sea conditions. The Tp values used in the simulation study fall within this range. Table 15 illustrates the six sea conditions, including the platform without CH and with CH surge, heave, and pitch, as well as the mean peak-to-trough distance from the WWF and WEC-Sim. The RMSE between the WWF and WEC-Sim results was 0.174 for surge, 0.247 for heave, and 0.263 for pitch. Amongst

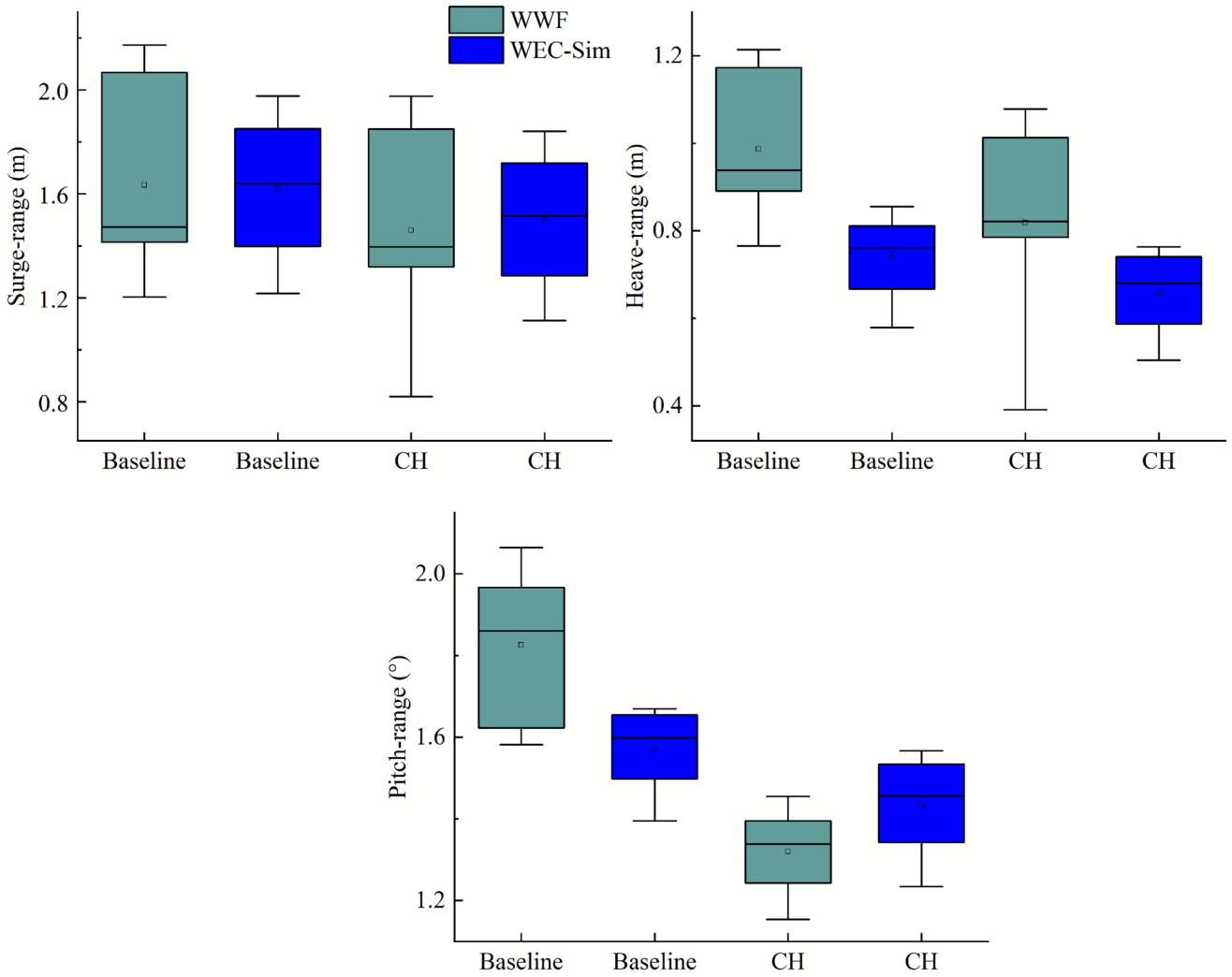

Fig. 17 Boxplots with the mean peak-to-trough distances for the baseline platform without CH and with CH for surge, heave, and pitch motions in RWW in the WWF and WEC-Sim

Table 15 Surge, heave and pitch mean peak-to-trough distance results in the WWF and WEC-Sim across ten sea conditions for the baseline platform and with CH

Sea condition	FOWT	Surge (m)		Heave (m)		Pitch (°)	
		WWF	WEC-Sim	WWF	WEC-Sim	WWF	WEC-Sim
1	Baseline	1.204	1.217	0.765	0.579	1.967	1.395
	CH	0.819	1.113	0.391	0.504	1.243	1.234
2	Baseline	1.414	1.399	0.890	0.667	1.758	1.498
	CH	1.343	1.285	0.785	0.587	1.395	1.342
3	Baseline	1.506	1.566	0.954	0.736	1.623	1.573
	CH	1.448	1.443	0.839	0.654	1.348	1.425
4	Baseline	1.438	1.715	0.932	0.783	1.582	1.624
	CH	1.319	1.587	0.802	0.706	1.154	1.488
5	Baseline	2.067	1.851	1.173	0.811	2.064	1.655
	CH	1.849	1.719	1.013	0.741	1.455	1.534
6	Baseline	2.173	1.977	1.214	0.855	1.963	1.670
	CH	1.975	1.841	1.149	0.763	1.328	1.567

Table 16 Mean peak-to-trough distance and max pitch at site A

Sea condition	FOWT	Surge (m)	Heave (m)	Pitch (°)	Max pitch backwards (°)
1	Baseline	0.308	0.060	0.127	4.810
	CHS	0.278	0.042	0.104	4.189
2	Baseline	0.415	0.150	0.309	3.858
	CHS	0.383	0.113	0.283	3.373
3	Baseline	0.561	0.213	0.696	4.499
	CHS	0.527	0.186	0.639	3.942
4	Baseline	4.810	1.368	3.907	5.621
	CHS	4.617	1.308	3.915	5.132
5	Baseline	3.373	1.198	3.130	5.507
	CHS	3.224	1.136	3.057	4.970
6	Baseline	2.580	0.983	2.596	5.336
	CHS	2.456	0.934	2.506	4.783

these, surge showed the best agreement with the experimental values, followed by heave and then pitch. Additionally, Fig. 17 shows the surge, heave, and pitch boxplots, which contain the mean peak-to-trough distances of the WWF and WEC-Sim in RWW, presented in Table 15. Each boxplot displays the distribution of values, where the box represents the interquartile range, the line inside the box indicates the median, the whiskers denote the data spread, and the square marker represents the average value.

The differences between the experiment and simulation results can be attributed to several factors. WEC-Sim is based on linear potential flow theory, which assumes the fluid is inviscid and irrotational, and does not account for viscous effects, turbulence, or nonlinear wave–structure interactions. The aerodynamic loads on the platform are computed using MOST, which applies blade element momentum theory and assumes a uniform wind flow over the rotor. However, it does not model unsteady aerodynamic effects, turbulence, or flow separation, which may contribute to discrepancies when compared to experimental results. In contrast, the WWF experiments capture the full physical behaviour of the scale model under combined wave and wind loading. These tests include the effects of the mooring line configuration, as well as nonlinearities, viscous damping, model-scale influences, and interactions with the flume's side walls. They also account for wind loads acting on the structure above the waterline, effects that are not fully captured in the numerical model. Despite these limitations, WEC-Sim provides a valid approximation of platform motions and serves as a tool for early-stage design and preliminary performance evaluations.

Appendix 4: Mean peak-to-trough distance, max pitch of platforms, and mooring restoring forces

The motion data for the FOWT without CH and with CHS at site A, including the mean peak-to-trough distances in surge, heave, and pitch, as well as the maximum backwards pitch angle, are shown in Table 16. It also includes the same results for site B, covering all configurations without CH and with CH, CHL, and CHS, illustrated in Table 17.

The restoring force characteristics of the mooring line systems at sites A and B, computed in WEC-Sim for surge, heave, and pitch simulations, are presented in Fig. 18. Although the detailed analysis of mooring restoring forces was not the primary objective of this study, these results are included to complement the motion assessment and provide additional insight into the system behaviour. Figure 18a–c shows the restoring forces in surge, heave, and pitch at site A, whilst Fig. 18d–f presents the corresponding results for site B. The differences observed between the two sites are mainly attributed to variations in mooring line length, anchor location, horizontal distance from the fairlead to the anchor, and water depth.

Table 17 Mean peak-to-trough distance and max pitch at site B

Sea condition	FOWT	Surge (m)	Heave (m)	Pitch (°)	Max pitch backwards (°)
1	Baseline	0.261	0.052	0.105	3.825
	CH	0.228	0.036	0.070	3.348
	CHL	0.225	0.033	0.068	3.282
	CHS	0.236	0.037	0.086	3.351
2	Baseline	0.489	0.191	0.623	4.215
	CH	0.444	0.154	0.528	3.688
	CHL	0.439	0.148	0.516	3.615
	CHS	0.458	0.172	0.573	3.706
3	Baseline	1.077	0.470	1.386	4.377
	CH	0.980	0.403	1.194	3.827
	CHL	0.971	0.391	1.176	3.753
	CHS	1.014	0.481	1.305	3.877
4	Baseline	5.576	2.281	4.735	5.353
	CH	5.191	2.135	4.442	4.832
	CHL	5.156	2.117	4.452	4.780
	CHS	5.316	2.469	4.810	5.005
5	Baseline	4.139	1.885	3.900	5.086
	CH	3.828	1.701	3.575	4.534
	CHL	3.800	1.670	3.569	4.472
	CHS	3.931	1.951	3.884	4.676
6	Baseline	3.341	1.556	3.267	5.033
	CH	3.082	1.389	2.967	4.460
	CHL	3.058	1.360	2.956	4.393
	CHS	3.168	1.593	3.226	4.579

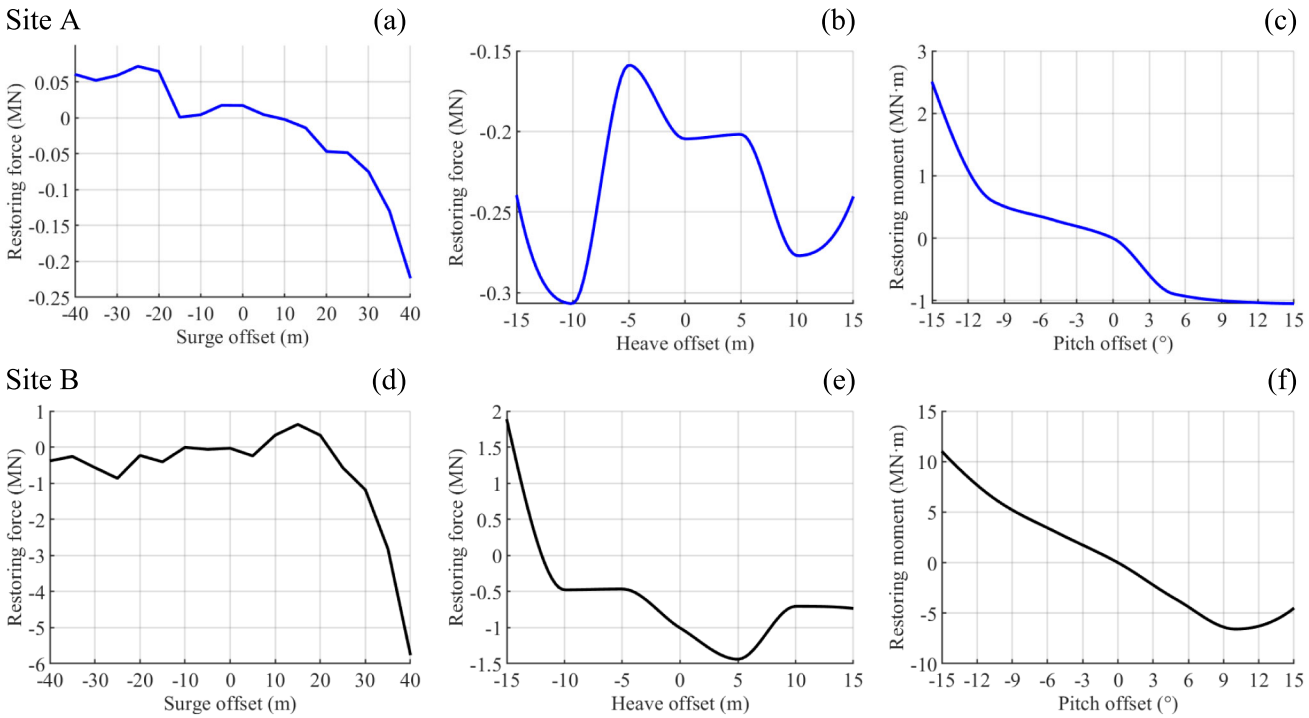

Fig. 18 Restoring force characteristics of the OC4-DeepCwind catenary mooring system in surge, heave, and pitch motions: **a–c** site A; **d–f** site B

Acknowledgements Diego F. Bernal-Camacho thanks the CONAHCYT and University of Groningen Scholarship support for PhD studies at II-UNAM and UG. Jassiel V. H. Fontes thanks the support provided by Fundação de Amparo à Pesquisa do Estado do Amazonas through Programa FAPEAM Produtividade em CT&I—Edição 2024 (Edital nº 020/2024).

Author contributions D.B.: conceptualisation, methodology, formal analysis, investigation, writing—original draft, visualisation. E. M.: resources, supervision, writing-review and editing, project administration. J. H.: writing-review and editing. C.E: image analyses, methodology. A. V.: supervision, writing-review and editing.

Funding Funding was supported by the Secretaría de Ciencia, Humanidades, Tecnología e Innovación (SECIHTI).

Data availability Data can be provided upon request.

Declarations

Conflict of interest The authors declare no competing interests.

References

Abbas NJ, Zalkind DS, Pao L, Wright A (2022) A reference open-source controller for fixed and floating offshore wind turbines. Wind Energ Sci 7:53–73

Aboutalebi P, M'zoughi F, Garrido I, Garrido AJ (2023) A control technique for hybrid floating offshore wind turbines using oscillating water columns for generated power fluctuation reduction. J Comput des Eng 10:250–265

Anderson JD (2011) Fundamentals of aerodynamics, 5th edn. McGraw-Hill Higher Education, New York

Bernal-Camacho DF, Mendoza E, Fontes JVH et al (2024) Experiments in an enclosed wave--wind flume environment to study the dynamics of a small-scale floating offshore wind turbine. J Ocean Eng Mar Energy 1–23

Borg M, Utrera Ortigado E, Collu M, Brennan FP (2013) Passive damping systems for floating vertical axis wind turbines analysis. In: European wind energy conference. Vienna, Austria, pp 3–7

Burton T, Jenkins N, Sharpe D, Bossanyi E (2001) Wind energy handbook, 2nd edn. John Wiley & Sons, New York

Capaldo M, Mella P (2022) Damping analysis of floating offshore wind turbine (FOWT): a new control strategy reducing the platform vibrations. Wind Energy Sci Discuss 2022:1–29

Chakrabarti SK (1994) Offshore structure modeling, vol 9. World Scientific, Singapore

Chitteth Ramachandran R, Desmond C, Judge F, Serraris JJ, Murphy J (2022) Floating wind turbines: marine operations challenges and opportunities. Wind Energy Sci 7(2):903–924. https://doi.org/10.5194/wes-7-903-2022

Collu M, Maggi A, Gualeni P et al (2014) Stability requirements for floating offshore wind turbine (FOWT) during assembly and temporary phases: overview and application. Ocean Eng 84:164–175. https://doi.org/10.1016/j.oceaneng.2014.03.018

Dagher JH, Goupee AJ, Viselli AM (2024) Optimized floating offshore wind turbine substructure design trends for 10–30 MW turbines in low-, medium-, and high-severity wave environments. Designs. https://doi.org/10.3390/designs8040072

EDF, and CEA (2022) SALOME Platform v.9.9.0. Computer Software. https://www.salome-platform.org/

Enevoldsen P, Permien F-H, Bakhtaoui I et al (2019) How much wind power potential does Europe have? Examining European wind power potential with an enhanced socio-technical atlas. Energy Policy 132:1092–1100

Ferrerire T, Rasb W (2012) ImageJ user guide. National Institutes of Health, USA. https://imagej.net/ij/docs/guide/user-guide.pdf

Flanders Marine Institute (2025) MarineRegions.org. https://www.marineregions.org/. Accessed 4 Apr 2025

Gonçalves RT, Malta EB, Simos AN, Hirabayashi S, Suzuki H (2023) Influence of heave plate on the flow-induced motions of a floating offshore wind turbine. J Offshore Mech Arct Eng 145:32001. https://doi.org/10.1115/1.4056345

Government.nl (2024) Offshore wind energy. Accessed: November. 29, 2024. https://www.government.nl/topics/renewable-energy/offshore-wind-energy. Accessed 29 Nov 2024

Guo C, Sheng W, De Silva DG, Aggidis G (2023) A review of the levelized cost of wave energy based on a techno-economic model. Energies 16:2144

Hall M, Goupee A (2015) Validation of a lumped-mass mooring line model with DeepCwind semi-submersible model test data. Ocean Eng 104:590–603

Hersbach H, Bell B, Berrisford P, Hirahara S, Horányi A, Muñoz-Sabater J, Schepers D (2020) The ERA5 global reanalysis. Q J R Meteorol Soc 146(730):1999–2049

Holthuijsen LH (2010) Waves in oceanic and coastal waters. Cambridge University Press, Cambridge

Hong S, McMorland J, Zhang H, Collu M, Halse KH (2024) Floating offshore wind farm installation, challenges and opportunities: a comprehensive survey. Ocean Eng 304:117793. https://doi.org/10.1016/j.oceaneng.2024.117793

Huang J, Xu H, Chen L, Lin K, Guo M, Yang M, Rui S (2024) Analysis of mooring performance and layout parameters of multi-segment mooring system for a 15 MW floating wind turbine. Front Energy Res. https://doi.org/10.3389/fenrg.2024.1502684

IRENA and GWEC (2023) Enabling frameworks for offshore wind scaleup: Innovations in permitting, International Renewable Energy Agency, Abu Dhabi. https://www.irena.org/-/media/Files/IRENA/Agency/Publication/2023/Sep/IRENA_GWEC_Enabling_frameworks_offshore_wind_2023.pdf

Jonkman J, Butterfield S, Musial W, Scott G (2009) Definition of a 5-MW reference wind turbine for offshore system development (No. NREL/TP-500-38060). National Renewable Energy Lab. (NREL), Golden, CO (United States). https://doi.org/10.2172/947422

Keivanpour S, Ramudhin A, Ait Kadi D (2017) The sustainable worldwide offshore wind energy potential: a systematic review. J Renew Sustain Energy 9:065902

Kurnia R, Ducrozet G (2022) NEMOH V3. 0 user manual. Ecole Centrale de Nantes. https://www.researchgate.net/profile/Ruddy-Kurnia/publication/366166860_NEMOH_v30_User_Manual/links/63942c1a484e65005bfa7ec2/NEMOH-v30-User-Manual.pdf

Li H, Zheng J, Zhang J, Peng W, Peng J (2024) Numerical investigation on dynamic responses of a semi-submersible wind turbine with different types of heave plates. Ocean Eng 310:118650. https://doi.org/10.1016/j.oceaneng.2024.118650

Lian Y, Zhong F, Zheng J, Chen W, Ma G, Wang S, Yim SC (2023) Effects of mooring line with different materials on the dynamic response of offshore floating wind turbine. J Mar Sci Eng 11(12):2302. https://doi.org/10.3390/jmse11122302

Martinez A, Iglesias G (2024) Levelized cost of energy to evaluate the economic viability of floating offshore wind in the European Atlantic and Mediterranean. E-Prime Adv Electr Eng Electron Energy 8:100562

Masciola M, Jonkman J, Robertson A (2013) Implementation of a multisegmented, quasi-static cable model. In: ISOPE international ocean and polar engineering conference, Anchorage, Alaska, p ISOPE–I

Netherlands Ministry of Defence (2025) Exclusive economic zone. https://english.defensie.nl/downloads/applications/2025/04/25/exclusive-economic-zone. Accessed 4 Apr 2025

Newman JN (2018) Marine hydrodynamics. The MIT Press, Cambridge

Porto Tapiquen CE (2017) Europe. In: Bases on shapes from Environmental Systems Research Institute (ESRI). Free distribution. http://tapiquen-sig.jimdo.com. Accessed 4 Apr 2025

Robertson A, Jonkman J, Masciola M, Song H, Goupee A, Coulling A, Luan C (2014) Definition of the semisubmersible floating system for phase II of OC4 (No. NREL/TP-5000-60601). National Renewable Energy Lab.(NREL), Golden, CO (United States). https://doi.org/10.2172/1155123

Rueh K, Keester A, Ströfer CAM, nathanmtom, Topper M, Lawson M, Husain S, Ling BA, Ogden D, Leon J, Nguyen L, Alves EF, SiHeTh. (2024). WEC-Sim/WEC-Sim: v6.0 (v6.0). Zenodo. https://doi.org/10.5281/zenodo.10023797

Sirigu M, Faraggiana E, Ghigo A, Bracco G (2022) Development of MOST, a fast simulation model for optimisation of floating offshore wind turbines in Simscape Multibody. J Phys Conf Ser 2257:12003

Sirnivas S, Yu Y-H, Hall M, Bosma B (2016) Coupled mooring analyses for the WEC-Sim wave energy converter design tool. In: International conference on offshore mechanics and arctic engineering, Busan, South Korea, p V006T09A023

Sovacool BK, Enevoldsen P (2015) One style to build them all: corporate culture and innovation in the offshore wind industry. Energy Policy 86:402–415

Stockhouse D, Phadnis M, Grant E, Johnson K, Damiani R, Pao L (2022) Control of a floating wind turbine on a novel actuated platform. In: 2022 American control conference (ACC), Atlanta, GA, USA, pp 3532–3537

Subbulakshmi A, Sundaravadivelu R (2021) Effects of damping plate position on heave and pitch responses of spar platform with single and double damping plates under regular waves. Ocean Eng 224:108719

Timmington D, Efthimiou L (2022) Mooring systems for floating offshore wind: integrity management concepts, risks and mitigation. In: World Forum Offshore Wind. https://wfo-global.org/wp-content/uploads/2023/01/Mooring-Systems-White-Paper.pdf

WSP UK Limited HAS and AL (2025) CampionWind Offshore Wind Farm Array Area—Environmental Impact Assessment, Scoping Report Appendices https://marine.gov.scot/sites/default/files/appendices_0.pdf

Weller S, Gueydon S (2012) Analysis of the DeepCwind model tests and a first attempt to simulate a semi-submersible floating wind platform with aNySIM: final report: https://doi.org/10.13140/RG.2.2.14465.56168

Yang W, Han Y, Ma R, Hou M, Yang G (2023) A composite super-twisting sliding mode approach for platform motion suppression and power regulation of floating offshore wind turbine. J Mar Sci Eng 11(12):2318. https://doi.org/10.3390/jmse11122318

Yang L, Jiang Y, Guo S, Lin Z, Deng W, Liu L (2024) Research on the effect of a heave plate on the dynamics of the floating wind turbine using model tests. J Mar Sci Eng 12(10):1808. https://doi.org/10.3390/jmse12101808

Zhao J, Zhang L, Wu H (2012) Motion performance and mooring system of a floating offshore wind turbine. J Mar Sci Appl 11:328–334

Zhao H, Wu X, Zhou Z (2024) Exploring motion stability of a novel semi-submersible platform for offshore wind turbines. Energies 17:2313

Zhu H, Hu C, Sueyoshi M, Yoshida S (2020) Integration of a semisubmersible floating wind turbine and wave energy converters: an experimental study on motion reduction. J Mar Sci Technol 25:667–674